View Article Online
View Journal

Nanoscale Horizons

The home for rapid reports of exceptional significance in nanoscience and nanotechnology

Accepted Manuscript

This article can be cited before page numbers have been issued, to do this please use: S. Shyam, S. Han, H. Shim and T. Kim, *Nanoscale Horiz.*, 2026, DOI: 10.1039/D6NH00127K.

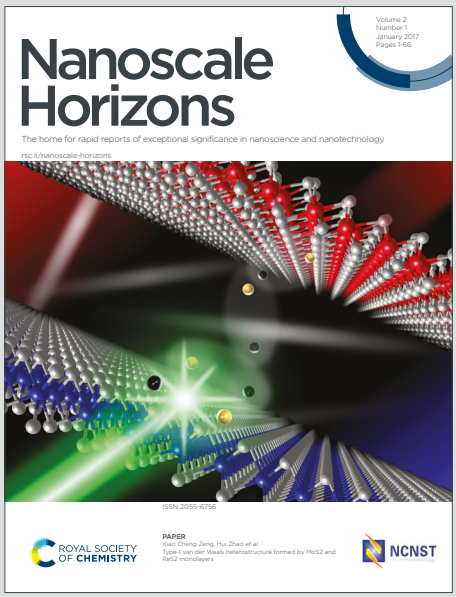

Fundamental and Technical Advances in Bulk Photovoltaics of 2D van der Waals Materials

View Article Online
DOI: 10.1039/D6NH00127K

*Sukalyan Shyam[1], Sujeong Han[2], Hyunwoo Shim[2], Taesung Kim[1,2,3]**

[1]School of Mechanical Engineering, Sungkyunkwan University (SKKU), Suwon, 16419 Republic of Korea

[2]Department of Semiconductor Convergence Engineering, Sungkyunkwan University (SKKU), Suwon, 16419, Republic of Korea

[3]SKKU Advanced Institute of Nano Technology and Department of Nano Science and Technology (SAINT), Sungkyunkwan University, Suwon, 16419, Republic of Korea

Abstract

2D van der Waals (vdW) materials with exceptional electronic and optical properties have emerged as a hotspot of materials science research. Over the last few years, substantial growth has been observed in the engineering of these materials for the bulk photovoltaic effect (BPVE). BPVE is the conversion of electricity from light via an entirely distinct mechanism from the *pn* junction photovoltaic device. The ability of tunable crystal structure, maintaining clean interfaces, and the feasibility of easy creation of heterostructures and heterojunctions of 2D vdW materials allows for the manipulation of crystal symmetry, electronic polarization, light-matter interaction, and more, leading to the efficient engineering of BPVE. A critical discussion of the fundamentals of engineering the BPVE using different material systems and innovative strategies has been made based on the previous scientific reports. The key challenges that can hinder device efficiency are also covered. The potential for a next-generation, self-powered, energy-efficient, flexible, and lightweight device utilizing the BPVE of 2D vdW materials is highlighted in this article.

Keywords: Bulk photovoltaic effect (BPVE); 2D vdW materials; ferroelectric; flexo-photovoltaic; piezo-Photovoltaic; Shift current; photo galvanic effect (PGE); depolarization field; broken symmetry

* Author to whom all correspondence should be addressed,
E-mail (T. Kim): tkim@skku.edu
ORCID iD: https://orcid.org/0000-0001-6280-7668

View Article Online
DOI: 10.1039/D6NH00127K

1. Introduction

Photovoltaics is one of the most precious technologies in the world, which directly converts light energy into electrical energy. The most successful category of photovoltaic technology is silicon *pn* junction solar cells, where a built-in electric field at the junction of two differently doped materials facilitates the separation of generated electron-hole pairs upon absorption of photons with energy higher than the material's band gap [1]. Unlike *p-n* junction photovoltaics, the bulk photovoltaic effect (BPVE) converts light energy into electricity without any built-in electric field [2]. The band gap does not limit the maximum open-circuit voltage (V_{OC}) in BPVE due to its quantum mechanical origin [3]. Theoretically, it can exceed the Shockley-Queisser limit on power conversion efficiency, a major constraint in traditional *p-n* junction photovoltaics [4].

The origin of BPVE is widely attributed to the nonlinear interaction of light with polarized materials, particularly those with asymmetric crystal structures. The current generated by BPVE mainly consists of: shift current or linear photo galvanic effect (LPGE), which depends on linearly polarized light [5], circular photo galvanic effect (CPGE), which depends on the helicity of light and becomes zero under linearly polarized illumination [6]. Another mechanism mentioned in the literature is the depolarization (DEP) field between two electrodes [7].

BPVE is first observed in perovskite material and has been extensively explored in the last few decades. It was probably first observed by A.G. Chynoweth in 1956 in Barium Titanate, which produces pyroelectric current without the application of an electric field [8]. Consecutive works by F.S. Chen, A.M. Glass *et al.,* and others reported this current in similar categories of crystal systems. Subsequently, this effect was named the BPVE [9–11]. Bulk perovskites have been widely investigated for BPVE; however, the wide band gap restricts the absorption of low-energy photons in these perovskite materials, and this phenomenon is essentially limited to low-wavelength light [12–16].

In recent years, the BPVE has emerged as a compelling topic in the field of 2D Van der Waals (vdW) material research. Due to their tunable atomic-scale dimensions, adjustable crystal symmetry, and versatile electronic and optical properties, 2D vdW materials offer a unique platform for exploring and enhancing BPVE [17–19]. This growing interest is driven by the potential to develop highly efficient BPVE-based devices for real-world applications and deepen our understanding of the fundamental mechanisms behind the effect. 2D vdW materials offer distinct advantages for specialized applications, including advanced optoelectronic devices, high-density synaptic devices for in-memory computing, and high-power-density

View Article Online
DOI: 10.1039/D6NH00127K

flexible nanogenerators, key technologies that support the widespread adoption of the Internet of Things (IoT). For the first time, significant photocurrent generation without *p-n* junctions has been observed in layered vdW GeS by Kushnir et al. in 2017 [20]. Since then, BPVE in vdW layered materials has been extensively studied in various systems, such as 3R-MoS_2, 1T'-ReS_2, $CuInP_2S_6$ (CIPS), In_2Se_3, and many more [21–24]. Although broken inversion symmetry or a noncentrosymmetric crystal structure is the key requirement of BPVE, it can also be artificially induced in symmetric 2D materials through the reduction of symmetry in the system via strain engineering, defect introduction, and other methods [25,26]. Due to their atomic thickness, 2D vdW materials are feasible for manipulating crystal symmetry, possess defect-free surface states, exhibit good charge carrier mobility, and feature a spectrum of band gaps ranging from a few meV to a few eV. Additionally, an easy fabrication procedure, along with a reduced requirement for expensive and high-maintenance instruments, supports the investigation possibility on different systems and in various device architectures.

In recent review articles on BPVE in vdW materials, although symmetry and crystal structures are discussed intriguingly, the systematic discussion of the fundamental mechanisms underlying the effect and its limitations in these materials remains lacking. In a review paper, only the BPVE effect in TMDCs is considered; however, it also occurs in monochalcogenides and Weyl semimetals. Therefore, this review concerns the fundamental causes, limitations, carefully categorized material systems (those that require external stimulation and those that do not), technical advancements, key challenges, and the most valuable application purposes. Moreover, previous reviews focused on the possibility of surpassing the Schottky-Queisser (SQ) limit by BPVE; however, BPVE is also constrained by other critical issues covered in this article.

After the introduction section, a brief explanation of the fundamental mechanisms and measurement procedures is provided. Then, a comprehensive discussion of various reported BPVE-active materials and engineering strategies is presented; majorly categorized into (i) BPVE in intrinsically asymmetric material: only the materials that generate BPVE without any external influence; (ii) Strain-induced BPVE: Artificially breaking symmetry; (iii) Other strategies. The key challenges that can hinder device efficiency are subsequently addressed. Finally, the conclusion and outlook section contains the future directions and recommendations for utilizing this novel energy conversion mechanism. The historical evolution of notable discoveries of BPVE in 2D vdW materials is presented in Fig. 1(a). Additionally, a schematic representation of the BPVE observed in different materials using various techniques, which are also covered in this article, is depicted in Fig. 1(b).

View Article Online
DOI: 10.1039/D6NH00127K

2. Mechanism of BPVE

Before exploring the advancements of BPVE in 2D vdW materials, it is important to briefly understand the mechanisms behind its three distinct origins and their significant limitations. This section aims to provide readers with a clear and concise overview of this effect.

a. LPGE: Shift Current

Quantum mechanically, the electron wave packet acquires a geometrical phase shift as it moves in k-space of a solid, known as the Berry phase [27]. In noncentrosymmetric materials, the lack of inversion symmetry gives rise to distinct Berry connections (Berry connection is a mathematical quantity which defines the change of a quantum state as it moves through the k-space, and its integral in a closed loop quantifies the Berry phase) in the conduction and valence bands [23]. When electrons are optically excited across the band gap, this difference produces a real-space displacement of the electron wave packet because of the distinct Berry connection of the energy bands, known as the shift vector, during the inter-band transition, as depicted in Fig. 2(a) [28,29]. The resulting spatial separation of photoexcited carriers after multiple successive ballistic transport events causes the carrier to reach the electrode, as shown at the bottom of Fig. 2(a). It generates a finite photocurrent under continuous illumination, referred to as the shift current [30]. These carriers are non-thermalized due to the extremely fast transit of photogenerated carriers to the electrodes [31], making them immune to the Shockley-Queisser efficiency limit of p-n junction solar cells, offering the possibility of surpassing it.

Since the Berry connection depends on the polarization angle of the incident light, it leads to a polarization-dependent shift current, as shown in Fig. 2(d) [32,33]. The spontaneous electrical polarization of the crystal is fundamentally linked to the shift current; however, strong polarization does not always generate a large shift current [5]. In crystals, electrical polarization involves both ion displacement and the electronic part (asymmetry in covalent bond wave functions), which is associated with the Berry phase, as per the modern theory of polarization [34]. Thus, the shift vector is also associated with the electronic polarization of the material, and materials with strong electronic polarization could be compelling for shift current generation [35,36]. The large spontaneous polarization in 2D vdW materials can be dominated by ionic displacements driven by anharmonic lattice modes, where ionic positions change strongly, whereas the Wannier centers (center of charge localization) move little relative to the ions [37]. If Wannier centers are pinned to bonds, and the system has small Born effective charges (Z^*), it results in weak Berry-phase redistribution and limited shift current. In contrast, material which exhibits high Z^* and enhanced Berry curvature near the band edge, supporting strong shift

View Article Online
DOI: 10.1039/D6NH00127K

current even when the net polarization is moderate [38]. Therefore, the Z^*, Berry curvature, and Wannier center could be predictive descriptors for selecting the material system, rather than the system's net polarization. This quantum-coherent mechanism, which can also be described as the motion of dipoles in momentum space driven by photon momentum transfer, provides a pathway toward next-generation photovoltaic and optoelectronic devices with efficiencies beyond conventional limits. In 2D vdW ferroelectrics, because of the intrinsic polarization axis that guides the transport of carriers after Berry phase-driven separation, the shift current tensors, which play a crucial role in generating photocurrents, retain nonzero components even when exposed to unpolarized light. As a result, these materials can achieve asymmetric excitation even in unpolarized light. In contrast, nonpolar materials, even if they are noncentrosymmetric, do not exhibit spontaneous polarization and thus lack inherent directionality. For these materials, the shift current response relies completely on the polarization of the incoming light to create symmetry breaking in the excitation process. Consequently, unpolarized light, which effectively averages over multiple directions, does not lead to a net shift current in these nonpolar materials. [28,39,40]. Hence, materials lacking symmetry, although nonpolar, exhibit the shift current only when interacting with polarized light. In contrast, ferroelectric materials that possess crystal asymmetry, as well as a spontaneous polarization state, exhibit the shift current even with unpolarized light [5].

b. CPGE

It can be illustrated by the example of the crystal symmetry of the most famous 2D vdW material, MoS_2. The material with broken inversion symmetric material, like monolayer MoS_2, possesses valley contrast spin splitting in the valence band maxima caused by the strong spin-orbit coupling, and co-location of conduction band minima and valence band maxima is at the same K point, as depicted on the top of Fig. 2(b) [41]. K-valley is coupled to positive electronic spin, and –K(K')-valley is coupled to negative electronic spin [bottom of Fig. 2(b)], known as spin-valley locking. Because of these fundamental characteristics, optical transitions occur selectively under the application of circular polarized light; right-handed circular polarized light (RCP) or positive helicity excites the electron in K^+, and left-handed circular polarized light (LCP) or negative helicity excites the electron in K^- [6,42]. Therefore, applying a specific helicity light generates an imbalance in the electron population between the two valleys. Now, broken inversion symmetry in MoS_2 leads to nonzero Berry curvature (Berry curvature is the curl of Berry connection), and time reversal symmetry ensures the equal but opposite Berry curvature in two valleys [43]. Nonzero berry curvature induces anomalous velocity in the generated

View Article Online
DOI: 10.1039/D6NH00127K

photoelectron transverse to the electric field. Therefore, circularly polarized light with a finite net current creates an imbalance of electrons in two valleys, even though the Berry curvature simulates the generated photoelectron in the opposite direction. With varying chirality of the light, a periodic variation of the CPGE effect induces a photocurrent produced with the highest/lowest for right-circular/left circular polarization because of selective excitation of the carrier in the material with broken spatial inversion symmetry, as shown in Fig. 2(e). In comparison, applying unpolarized and linearly polarized light, both valleys are populated with a similar number of electrons, which is canceled out by the opposite flow of carriers dictated by the equal but opposite Berry curvature in the two valleys [6,41]. Although the circular photo current is also generated in the Weyl semimetal via a subtly different process, the fundamental mechanism is similar to that discussed above. The detailed mechanism of the CPGE in Weyl semimetal will be addressed in the BPVE in the Weyl semimetal section.

c. DEP field-induced BPVE

The DEP field-induced self-bias photocurrent is observed in materials with spontaneous polarization. For example, as presented at the top of Fig. 2(c), α-In_2Se_3 with down polarization, bound charges are induced at the graphene interface as indicated by black + and – at the bottom and top graphene electrode, respectively, and these bound charges induce opposite image charges in the Graphene as shown by the white + and – signs. Incomplete screening of the bound charges leads to a DEP field that originates from the low carrier density of Graphene and is often reduced in the case of a thick metal electrode, which generates a current flow antiparallel to the polarization [24]. In the bottom of Fig. 2(c), a band diagram of the device under this DEP field is depicted. The slope is induced by the presence of the DEP field against the direction of the polarization force, which causes the drift of the photogenerated electrons and holes in opposite electrodes, leading to the photocurrent [44]. Unlike the shift current, the maximum V_{OC} in the DEP field-induced photovoltaic effect is not immune to the band gap of the active layer, according to the relationship [24]:

$$V_{OC} = \frac{E_g}{q} - HE_{DEP}$$

Where E_g is the band gap of the active layer, H is the thickness, and E_{DEP} is the DEP field. The V_{OC} will always be smaller than the band gap of the active layer, as the DEP field-induced photovoltaic effect follows a similar process to that of a *pn* junction, and as shown in Fig. 2(e) for DEP field-induced photocurrent in $Pb(Zr_{0.2}Ti_{0.8})O_3$ [45], it sometimes exhibits similar characteristics to those of a *pn* junction solar cell. However, if the shift current substantially

View Article Online
DOI: 10.1039/D6NH00127K

influences the device performance, it may surpass this limitation in some cases. It is worth noting that no vdW photovoltaic device has approached the band-gap limit of V_{OC} to date, as contact resistance and bulk leakage keep V_{OC} well below the material's band gap. For instance, in the In_2Se_3 device, the V_{OC} is far below the band gap and increases at lower temperatures as the bulk resistance increases [46]. High contact resistance is often induced by interface defects and Fermi-level pinning; for instance, in edge contacts with a Bi semimetal on 3R-MoS_2, this increased the device's V_{OC} and short-circuit current [47]. Therefore, more studies on contact engineering and bulk resistance optimization in 2D vdW photovoltaics would be a valuable addition to the literature. A comparison between different mechanisms of BPVE is presented in Table 1.

Table 1. Comparison between LPGE, CPGE, and DEP field-induced BPVE.

	LPGE	CPGE	DEP field-induced
Physical Origin	Real-space displacement of the electron wave packet facilitated by the distinct Berry connection of the energy bands.	Nonzero berry curvature induces anomalous velocity in the generated photoelectron transverse to the electric field.	Incomplete screening of bound charges induces the DEP field.
Material system requirement	Non-centrosymmetric crystal structure with/without spontaneous polarization. Monochacogenides, TMDCs, Post Transition metals chalcogenides	Non-centrosymmetric crystal, along with strong Spin-orbit coupling Monolayer TMDC and Topological Weyl's semimetals are strong candidates.	Material with spontaneous polarization. Low carrier density Graphene as an electrode to ensure incomplete screening of bound charge. TMDC Post Transition metal chalcogenides
Device structure	Typically lateral	Typically lateral	Only Vertical
Constraint of V_{OC}	Theoretically, V_{OC} is not limited and can exceed the SQ limit; however, the fill factor is limited to 25%.	Similar to LPGE.	V_{OC} is limited by the material's band gap and the induced DEP field. It can not exceed the SQ limit.
Direction control	Possible to smoothly control by varying the polarization angle.	Possible to smoothly control by varying the helicity of the light.	Polarization independent.
Key limitation	Current direction and magnitude depend heavily on the Crystal symmetry and Orientation of the light	Requires a high-quality chiral system, which often suppresses the signal.	Limited by the bound-charge screening effects and highly dependent on the electrode material.

View Article Online
DOI: 10.1039/D6NH00127K

	polarization relative to crystal axes.		
Focused application zone	Bias-free polarization-sensitive photodetector for secure communication and biomedical imaging.	Low-energy chiral photo detection. Highly promising for low-cost, energy-efficient microwave and terahertz detection.	Energy-efficient, high-density photodetector enabled by vertical and self-bias operation. Energy-efficient optoelectronic synaptic device. Solar energy harvesting.

3. How to characterize BPVE

BPVE devices can be fabricated in a lateral or vertical configuration. As discussed in the previous subsection, for lateral devices, the Berry phase or Berry curvature-induced current often dominates. In contrast, in the case of vertical devices, the DEP field-induced photovoltaic effect prevails, especially for 2D vdW materials. Two identical metal electrodes are placed over the active material in the lateral configuration. In a vertical configuration, the active material is sandwiched between two electrodes; however, special measures must be taken to inhibit unintentional contact between the top and bottom electrodes when working with these ultra-thin 2D materials. The unwanted Schottky barrier at the electrode material junction often misleads the BPVE characteristics. Apart from LPGE and CPGE, Schottky barriers act as a built-in potential, essentially generating current in either direction of the BPV current or in the opposite direction, and may create an elusive state to characterize. Therefore, it is important to minimize the influence of this Schottky barrier as much as possible for proper investigation. Previously, the author reported the adoption of a reflective Al layer to shade the electrode junction so that they can rule out the effect as shown in Fig. 2(i) [48]; however, in the application purpose, it builds in a potential-driven photocurrent in the same direction as the shift current, so it is unnecessary to eliminate the impact; rather, exploiting the Schottky barrier-induced current will improve conversion efficiency.

Usually, photocurrent mapping is an efficient tool, allowing the estimation of photocurrent at each point in the active material. Another way to confirm the BPVE effect of the device is to study the polarization-dependent photocurrent. The Schottky barrier is not responsive to the polarized light, and the photocurrent will be the same for all polarization

View Article Online
DOI: 10.1039/D6NH00127K

directions. In contrast, as the shift current strictly depends on the angle of polarization with respect to the crystal orientation of the active material, a distinct polarization-dependent current would be a feasible route to ensure the observed photovoltaic effect. The net generated photocurrent in BPV devices can be mathematically expressed as [48,49]:

$$J_i = G^l_{ijk} e_j e^*_k + iG^c_{ik}[ee^*]_k I$$

where the former component is linear bulk photovoltaic current, and the latter is circular photovoltaic current; I represents the intensity of the light; and component of polarization vector of light in x and y direction, denoted as e_i and e_k^*, respectively; $i[ee^*]$ signifies the level of circular polarization; and tensor component G^l_{ijk} and G^c_{ik} are linear and circular BPV coefficients, respectively. Suppose a linearly polarized light beam is applied to the device. In that case, the second part vanishes. The first part involves the vector multiplication of e_j and e_k. Therefore, by changing the polarization direction, we obtain a variable current, and from there, linear photocurrent coefficients can be determined. By adjusting the intensity of the applied light, it is also possible to measure the coefficient. The value of the components of the tensor elements depends on the crystal system [15].

A systematic identification of the shift current has been performed in SnS crystals by measuring photocurrent specifically at different positions, as reported by *Chang et al.* [48]. As shown in Fig. 2(i), the photocurrent measured at spots 1 to 4 of the SnS crystal, of which 1 and 4 are located near the electrodes, and the location of the black square spot is deep inside the electrode. The photocurrent under the electrode (the square black spot) is independent of polarization angle, while spots 1 to 4 are highly dependent on the polarization angle. Therefore, the photocurrent under the electrode is purely a Schottky barrier-induced current, as shown in Fig. 2(k). The polarization angle depends on the photocurrent at spots 1 and 4, which are completely different from spots 2 and 4, which are located deep inside the channel (Fig. 2(l)). Direction of strong polarized photocurrent on the armchair direction of the crystal when the polarization vector of light is parallel to the zigzag direction of the crystal, which is in good agreement with the theoretical calculation of the shift current vector. The abnormally strong polarized photocurrent direction at spots 1 and 4, which is mostly perpendicular to the measured current at spots 2 and 3, could be due to the combined effect of Schottky junction current and shift current. For example, the photocurrent at spot 4, possibly the shift current, is negative, and the Schottky junction current is positive. When these two are superimposed, they could generate a pattern if the magnitude of these two currents is on a similar scale. However, this change in photocurrent direction could also be caused by local strain induced by the metal electrode. A

View Article Online
DOI: 10.1039/D6NH00127K

few theoretical studies on GeSe and SnS have reported that, under strain, the shift current may change direction due to the alteration in the non-centrosymmetric atom arrangement [50,51]. Therefore, this type of measurement strategy is crucial for a better understanding of the fundamental origin of the observed photocurrent, thereby improving the device architecture.

The DEP field-induced current is independent of the polarization of light and often appears illusory in comparison to the Schottky barrier-induced current; however, it has a few key differences. Most importantly, the direction of photocurrent is easily alterable by flipping the polarization state of the ferroelectric material, as observed in the case of ReS_2. The depletion width and built-in field for Schottky junctions remain constant with variations in thickness, resulting in a constant V_{OC} across all thicknesses [45]. In contrast, the DEP field exhibits a significant increase in V_{OC} at elevated thickness. In Schottky junction and pn-junction photovoltaic devices, V_{OC} saturates at high power due to the series resistance; however, in a DEP field, substantial variations in V_{OC} exist even at high light intensities. Apart from those, the effect of the Schottky junction is generally reduced by using similar characteristics of the junction in both regions.

4. BPVE in intrinsically non-centrosymmetric 2D vdW without spontaneous polarization

The primary requirement for the BPVE is that the material have a noncentrosymmetric crystal structure; however, as discussed in the BPVE mechanism section, materials that lack an intrinsic polarization direction exhibit BPVE only under polarized light. The monolayer 2H-phase TMDCs, such as WS_2, MoS_2, WSe_2, and $MoSe_2$, lack inversion symmetry; however, because they lack intrinsic polarization, they generate shift current only under polarized light. The first principal studies have confirmed the existence of finite shift current in monolayer MoS_2 [52]. Similarly, ultrafast shift dynamics of the shift current in monolayer WS_2 have also been theoretically demonstrated in the literature [53]. These materials also exhibit CPGE due to strong spin-valley locking, supported by broken inversion symmetry and strong SOC, as discussed in the mechanism of CPGE section.

5. BPVE in intrinsically non-centrosymmetric 2D vdW with spontaneous polarization

This section will cover 2D vdW materials that are non-centrosymmetric, possess spontaneous electrical polarization, and can generate photocurrent under both unpolarized and polarized light.

View Article Online
DOI: 10.1039/D6NH00127K

a. Monochalcogenides

In 2015, it was theoretically predicted that Group IV vdW monochalcogenides monolayer, such as GeS, SnS, GeSe, and SnSe, exhibit strong in-plane ferroelectric properties because of puckered C_{2v} symmetric crystal structure, where elastic distortion happens as top and bottom atom in armchair direction spontaneously shifted in either x or y direction, as depicted in Fig. 3(a) for GeS [54,55]. These systems also possess moderate band gaps (1.8–2.3 eV in monolayer) [56]; altogether, these properties signaled the possibility of strong BPVE. Later in 2017, experimental evidence of the shift current in GeS was observed, even in a few-layer GeS layer, due to spontaneous surface polarization by the top-most layer [20]. Terahertz wave generation and linearly dependent shift current achieved in GeS nanosheet through photoexcitation with 400 nm light at normal incidence and at terahertz (THz) frequencies [Fig. 3(b)]. A few-layer SnS crystal can have different crystal structures, of which two types of layer arrangement, as shown in Fig. 3(c), anti-ferroelectric arrangement $\alpha(AB_{AFE})$, where polarization at adjacent layers vanishes. In contrast, in the case of ferroelectric $\beta'(AC_{FE})$ phase, spontaneous polarization is observed. These two phases coexist in the SnS crystal in different layers, as depicted in Fig. 3(d). Because of the spontaneous polarization from the $\beta'(AC_{FE})$ phase, a strong polarization-dependent photocurrent in the noncentrosymmetric material, a few-layer SnS, was observed [48]. This property indicates its promising potential as a third-generation photovoltaic device. It could also position it as a high-frequency photodetector due to its ultra-low shift carrier lifetime.

b. Dichalcogenides

2D transition metal dichalcogenides (TMDCs), particularly MoS_2, WS_2, and ReS_2, as well as their selenide counterparts, have been studied by a large number of laboratories due to their superior light absorption capabilities, which are attributed to their high exciton binding energy, remaining effective even at room temperature [57–59]. The role of excitons in BPVE is also theoretically calculated in monolayer GeS and MoS_2 [60]. As discussed in the section on the mechanism of BPVE, the crystal symmetry of the material plays a pivotal role in this phenomenon. TMDC material can exist in various crystal symmetries, such as 1H, 2H, 3R, and 1 T. Among these, 1H is a monolayer semiconducting material that is stable at room temperature, and inversion symmetry is broken. In comparison, 1T phase is metallic and metastable and can undergo phase transition to other metastable phases 1T', 1T'', and 1T'''. Bulk 1T is highly symmetric, but because of the lattice distortion, it often breaks symmetry, and depending on the strength of asymmetry, these are classified as 1T', 1T'', and 1T'''. It has been predicted that because of the narrow band gap of the 1T''' phase, with a highly asymmetric crystal structure

View Article Online
DOI: 10.1039/D6NH00127K

that induces spontaneous polarization, it can generate strong BPVE in a broad spectrum extending to near infrared wavelength [61]. The 2H phase is the stack for the 1H layer, and it also has a highly symmetric crystal structure, which is not active to BPVE.

In contrast, the rhombohedral stacked 3R-MoS_2 has broken inversion and mirror symmetry due to the sliding of one layer with respect to another, possesses spontaneous polarization in the out-of-plane direction known as sliding ferroelectricity, as shown in Fig. 3(e) -I and II [62]. Various scientific groups have utilized out-of-plane polarization of 3R-MoS_2 to generate DEP field-induced BPVE. For example, devices with 2 and 4 layers of 3R-MoS_2 sandwiched between two graphene electrodes demonstrated a self-biased photocurrent on the picosecond timescale as depicted in Fig. 3(f) [7]. Notably, the 2L 3R-MoS_2 device exhibits a recovery time as short as 17 ps, which is significantly slower than the charge transfer time observed at the MoS_2/graphene interface. In contrast, the recovery time for the four-layer device is markedly longer, suggesting contributions from slower components in thicker regions. This difference may occur from the presence of larger defects in 2D materials or the additional MoS_2-MoS_2 interfaces within the four-layer structure. The thermal relaxation during this slowdown may also result from charge transfer dynamics at the MoS_2/graphene interface, as evidenced by the stability of the recovery time in response to an external bias, similar to the behavior observed in the Gr/3L-WSe_2/Gr ultra-fast photodetector [63]. At a similar time, studies on 3R-MoS_2 reveal that photocurrent generation is independent of light polarization, suggesting that shift current phenomena do not dominate the photocurrent response; instead, the dominant mechanism is attributed to the DEP field [21]. There are two possible stacking domains in a 3R bilayer MoS_2 (Fig. 3(g)): in the AB domain, the molybdenum atom in the top layer is above the sulfur atom in the bottom layer, whereas in the BA domain, the same amount of shift happens along the opposite direction, rendering an in-plane mirror image. Furthermore, in both domains, the photocurrent decreased with increasing positive gate voltage, while for negative gate voltage, it decreased slowly, as depicted in Fig. 3(h), demonstrating that the photocurrent originates from the doping of graphene. The spontaneous polarization direction and PC polarity are opposite between these two domains [21].

While bulk ReS_2 is centrosymmetric, a few layers of ReS_2 can readily exhibit broken symmetry due to varying stacking orders of the 1T′ crystal structure (Fig. 3(e)-III). It maintains a strong excitonic feature even in a multilayer. In vertical configurations, the intrinsic symmetry of ReS_2 facilitates photovoltaic current generation through the dominant DEP field. However, the contribution of the shift current is also notable in the polarized photocurrent

View Article Online
DOI: 10.1039/D6NH00127K

illustrated in Fig. 3(i) [64]. Conversely, investigations of lateral few-layer ReS_2 devices with graphene contacts (Fig. 3(j)) have demonstrated strong shift current production, outperforming conventional lateral 2H- and 3R-MoS_2 devices due to reduced contact resistance with Graphene [22,26,65]. In contrast to bulk TMDC monolayers, which belong to the noncentrosymmetric D_{3h} point group with broken inversion symmetry and can generate self-biased photocurrent only under polarized light, WS_2 nanotubes present a unique case. Their curved surface introduces intrinsic strain (Fig. 3(e)-IV), resulting in broken mirror symmetry in the transverse direction (when WS_2 nanosheet rolled in zig-zag direction) that enables polarization and thereby BPVE generation even under unpolarized light, whether in single-wall or multi-wall configurations [40,66]. Additionally, Janus TMDCs, characterized by different chalcogens on opposing sides of the transition metal, can exist solely as single layers. This composition, exemplified in Fig. 3(l) for MoSSe, S, and Se, creates mirror asymmetry in the out-of-plane direction. The differing electronegativities of these chalcogens induce spontaneous polarization perpendicular to the layers [67,68]. Experimental observations have confirmed ultra-fast and high self-biased photocurrents arising from these out-of-plane intrinsic polarizations [68]. Furthermore, BPVE has been theoretically predicted in various Janus crystal structures composed of diverse transition metals combined with sulfur, selenium, and telluride [69,70]. Overall, TMDC is a popular platform for studying BPVE because of the diverse symmetry that stems from the different phases.

c. Other vdW Ferroelectrics: In_2Se_3, $CuInP_2S_6$, and SnP_2Se_6

BPVE is also continuously discovered in 2D vdW trinary and quaternary materials, such as CIPS and SnP_2Se_6, as well as in binary compounds like In_2Se_3, due to their strong intrinsic polarization supported by post-transition metals, which could enrich the field of BPVE. CIPS and SnP_2Se_6 produce ferroelectricity from the ionic displacement in each layer; on the other hand, In_2Se_3 produces ferroelectricity from the displacement of the atoms with respect to different layers. Cu atoms can exist in multiple stable positions, as demonstrated in Fig. 4(a), which generates spontaneous polarization [44]. For SnP_2Se_6, octahedral coordinated Sn–Se bonds lack hybridization, and the Sn–Se bonds are almost entirely ionic. The strong electron-withdrawing effect of the Se atoms gives rise to $Se^{2/3-}$, which remains displaced between the layers, thereby maintaining the integrity of SnP_2Se_6 and producing intrinsic polarization (Fig. 4(b)) [71]. As shown in Fig. 4(c), the In_2Se_3 crystal structure features a central Se atom displaced from the centrosymmetric position, resulting in both in-plane and out-of-plane polarization [46]. Most of the reported articles on In_2Se_3 and CIPS present the vertical device with top and bottom contacts, which is possible due to the higher intrinsic polarization of the materials in the out-of-

View Article Online
DOI: 10.1039/D6NH00127K

plane direction. As shown in Fig. 4(d), for an In_2Se_3-based vertical device, the signs of the short-circuit current and open-circuit voltage can be easily altered by applying a DC bias and flipping the material's polarization before measurement [23,72]. The role of the thickness of the active layer on the DEP field is also evident in the efficiency of the In_2Se_3 device depicted in Fig. 4(e) [24]. Efficiency decreased with increasing thickness, caused by a reduced DEP field; a similar characteristic is also observed for the CIPS [44]. In contrast, the contradiction of thickness (within 10 nm) dependent photocurrent using 3R-MoS_2 in vertical configuration, which increased efficiency has been observed, might be mainly evolved from the increase in photon absorption in the material with increasing thickness and overshades the effect of DEP field [73]. Therefore, the material's thickness plays an important role in photocurrent generation. With increasing thickness of vdW materials, optical absorption generally increases; however, interlayer carrier recombination after generation increases at higher thickness, while the DEP field decreases with increasing thickness and vanishes after a few layers. A qualitative phase diagram of the thickness dependence of BPVE is presented in Fig. 4(k). In a report on In_2Se_3 in a similar vertical structure, the temperature-dependent V_{OC} decreased with increasing temperature (Fig. 4(f)), revealing the influence of bulk resistance and contact resistance on the DEP field-dependent photovoltaic effect [46]. In the lateral configuration 2D SnP_2Se_6, a large first photocurrent in the μs range is observed through a shift current-generating mechanism, as confirmed in polarized photodetection, as shown in Fig. 4(h) and (j) [49]. A broad band photocurrent response (Fig. 4(i)) was also observed in SnP_2Se_6 because of the low band gap of 1.32 to 1.44 eV compared to the CIPS of 2.4–2.6 eV. Therefore, SnP_2Se_6 could be a more compelling material in the field of BPVE [49].

6. BPVE in topological vdW Weyl Semimetals

Nearly a century ago, H. Weyl proposed the existence of massless fermions characterized by definite chirality [74]. While such fundamental particles have not been detected in high-energy physics, condensed matter systems have recently provided an analog in the form of Weyl semimetals (WSMs). Energy level intersections at isolated points in momentum space exist in this material (Fig. 5(a) for $PtBi_2$ bulk crystal), known as a Weyl node, where low-energy excitations behave like Weyl fermions [75]. Each node carries a chirality ($\chi = \pm 1$), determined by the alignment of its spin with its momentum. Unlike Dirac semimetals, in which linear band crossing can be gapped out through the introduction of an extra mass term in the Hamiltonian, Weyl nodes are topologically protected, and it is not allowed to introduce any gap at the node

View Article Online
DOI: 10.1039/D6NH00127K

by external means [76,77]. Instead, in momentum space, Weyl nodes behave as monopoles of Berry curvature, and the topological charge of the monopole is chirality.

The singular Berry curvature near Weyl nodes also drives unconventional nonlinear optical phenomena. Among these, the CPGE has emerged as a powerful probe of chirality. CPGE arises because circularly polarized light couples selectively to Weyl nodes of a given chirality: for example, as shown in Fig. 5(b), RCP light propagating along the K_Z-axis induces optical transitions only on the $\chi = +1$ node at $+K_Z$ side, while LCP light excites the $-K_Z$ side to maintain the angular momentum conservation [78]. According to the characteristics of the Weyl cone, WSMs are subdivided into two categories: Type-I and Type-II. In type-I WSM, the upper cone and lower cone of the Weyl node meet the Fermi level only at a single point on the Fermi surface. In contrast, cones are tilted with respect to the Fermi surface in the case of a type-II Weyl, which leads to two sides of the Weyl node being asymmetric and helps to asymmetric excitation of the electrons, in contrast to the Type-I, where symmetric excitation of charge carriers between two Weyl nodes results in zero net current. A net photocurrent is produced if contributions from different nodes do not perfectly cancel. In WSMs with broken inversion symmetry, such as WTe_2, $MoTe_2$, $TaIrTe_4$, and TaAs, this interplay yields strong, nonvanishing CPGE responses over a broad spectral range [79,80]. In WSM, the linear dispersion relation is limited near the node. It fades away from the node; thus, the CPGE effect is only possible for low-energy photons, which can only excite the carrier in the linear dispersion zone. Suppose the Fermi level is far away from the node. In that case, it is not possible to generate the CPGE because the Pauli exclusion principle prohibits the existence of empty states and the associated transition, known as Pauli blockade. For instance, as shown in experimental evidence in Fig. 5(d), an anisotropic photocurrent measurement of the T_d-$TaIrTe_4$ crystal reveals that the anisotropy in photocurrent is very low for a lower wavelength of 633 nm, which induces charges far away from the Weyl node. In contrast, large anisotropies are observed for the 4 and 10.6 μm wavelengths due to the presence of a similar gap in the Weyl node [81]. So, having the Fermi level near the node is always better [82]. However, even in inversion symmetry-breaking WSM, the photocurrent vanishes if the perpendicular incidence of light still preserves the in-plane inversion symmetry.

Disorder in the system also plays a significant role; it introduces finite broadening of the energy bands, making them less sharp. This disorder broadening competes with Pauli blockade and might reduce its effect; however, charge-carrier scattering becomes substantial at room temperature and dominates the reduced Pauli Blockade effect, thereby weakening the

View Article Online
DOI: 10.1039/D6NH00127K

overall photo response [83]. If optical energy is comparable to the disorder broadening, multiple Weyl nodes contribute to the photocurrent, thereby modifying the practical lower bound for chiral-selective optical detection. In a clean sample, only one Weyl node contributes at a given photon energy. It generates the quantized CPGE, which can be destroyed or less pronounced due to disorder broadening [84].

In WTe_2, $MoTe_2$ type-II WSMs in crystal point group C_{2v} do not show second-order nonlinear shift current response under light incidents along the crystallographic c-axis, as shown in Fig. 5(c) [85,86]. These properties make WSMs an exciting materials platform. Their gapless, linearly dispersed bands enable broadband optoelectronic responses extending from the infrared to the terahertz regime. At the same time, their topological character enhances nonlinear effects near the Weyl nodes. In addition to CPGE, other nonlinear responses, such as second-harmonic generation and shift currents, are strongly influenced by the Berry curvature distribution and crystal symmetries. Together, these effects deepen our understanding of topological matter and open routes toward next-generation optoelectronic devices that exploit topology-driven robust photocurrents and light–matter interactions at the quantum level.

For the first time, mid-infrared photon detection was observed using the concept of Weyl semimetal in Type-I (TaAs) and Type-II ($TaIrTe_4$) Weyl semimetals [81,85,87]. Although it was previously discussed that in the case of type-I WSM, photocurrent vanished, the Fermi level or the chemical potential is never present at the node at room temperature, which produces a certain amount of asymmetry of photo excitation between two sides of the node, and utilizing this effect, circular polarized infrared light detection for 10.6 μm was demonstrated in type-I TaAs. In type-II $TaIrTe_4$ with tilted Weyl cone and creating tilted Fermi level by creating a built-in-electric field at the electrode junction, showing band structure at Weyl node, facilitating further imbalance of charge carriers, high photoresponsivity of 130.2 mAW^{-1} at 4 μm has been demonstrated, which is competitive to low temperature operated state-of-the-art MCT(HgCdTe) photodetector. So, these discoveries promise to replace the large, costly traditional infrared detectors. In WTe_2 type-II, robust photo response was observed at some specific edges of the material where C_{2v} symmetry breaks because of fracture along some crystallographic direction, as depicted in Fig. 5(f) [88]. It was further reported that observed photo responses possibly relate to the Fermi-arc type surface, even though the direction of fracture solely determines the survival of the generated photo carriers. Type-II WTe_2 also exhibits significant photo responses at large wavelengths of 4 and 10 μm. Due to strong spin-orbit interaction, the spin splitting in Te causes the crossing of nondegenerate bands from multiple Weyl cones in both the conduction

View Article Online
DOI: 10.1039/D6NH00127K

and valence bands, resulting in a different chirality selection rule. Recently, a systematic demonstration of wavelength-dependent photocurrent in Te has been shown in Fig. 5(g) [89]. For 4 μm, the wavelength-dependent photocurrent originated from the optical transition between two Weyl nodes at the valence band and conduction band, where the sensitivity for LCP light is higher as the right side of the node band is far away from the Fermi level. Whereas stronger RCP light sensitivity at a wavelength of ~10.6 is observed, an intra-band transition in the valence band, where only the left side is allowed for optical transition, because on the right side, both bands are buried deep under the Fermi level. On the contrary, the wavelength dependence of helicity at 4.5 μm is significantly reduced due to the non-matching of the required energy for band-to-band transition; nonetheless, a high photocurrent is observed, which may be attributed to thermal effects or anisotropy in the material.

7. Strain-induced BPVE

Artificially altering the symmetry of a material by strain can significantly enhance the shift current in noncentrosymmetric materials and can even generate the shift current in centrosymmetric materials [26,65]. According to the properties of applied strain, this phenomenon is known as piezo photovoltaic for uniform strain and Flexo photovoltaic for gradient strain [65,90,91]. Uniform strain can improve the asymmetry in polar or intrinsically asymmetric materials and enhance the BPVE. Unlike piezoelectricity, flexoelectricity is also observable in the symmetric crystal. Polar material converts to nonpolar material by applying a strain gradient. The induced polarization for strain gradient in the absence of an external electric field, expressed as a flexoelectric coefficient,

$$\mu_{ilm} = \frac{\partial P_i}{\partial \eta_{lmn}}$$

where, ($\eta_{lmn} = \partial u_{mn}/\partial x_i$ is the strain), u_{ilmn} is a fourth rank tensor, and the flexoelectric effect is symmetry allowed in any material. From a microscopic view, flexoelectricity includes two contributions: a lattice contribution due to internal atomic displacements based on a rigid-ion model and an electronic contribution due to charge-density redistributions induced by atomic displacements. In illustrating the microscopic mechanism of flexoelectricity, commonly, ionic pictures are considered, where rigid ions shift relative to each other and lead to polarization under the strain gradient, as depicted in Fig. 6(a) [92,93]. Therefore, Inversion symmetry can be lifted by strain gradient; subsequently, the BPV effect can also be manifested in centrosymmetric materials when coupled with the flexoelectric effect, which is termed the Flexo-PV (FPV) effect. A qualitative comparison can be drawn between the relationships

View Article Online
DOI: 10.1039/D6NH00127K

among ferroelectricity, piezoelectricity, and flexoelectricity, as shown in Fig. 6(b). Analogous to the fact that all ferroelectric materials exhibit piezoelectricity, while the converse is not true due to the absence of spontaneous polarization in many piezoelectric materials, all piezoelectric materials inherently exhibit flexoelectricity. However, only those materials belonging to crystal classes that break inversion symmetry can exhibit piezoelectric behavior. In the case of bulk crystal material, the amount of applicable strain gradient via bending is very low; thus, the flexoelectric effect is very difficult to realize. However, 2D materials are inherently flexible and can be easily bent, allowing for a large strain gradient to be achieved. Over the last few years, flexoelectric effects have been explored in these 2D materials by inventing different mechanisms to generate strain.

Monolayer 1H-MoS_2, which is noncentrosymmetric, has been shown to exhibit a substantial improvement in shift current when strain is applied in the y-direction in theoretical studies (Fig. 6(c)) [65]. Experimentally, the generation of shift current can be enhanced by inducing in-plane strain in MoS_2 by placing the film over pre-patterned gold electrodes, as illustrated in Fig. 6(e), which utilizes a microtrench to create uniform strain over the area where MoS_2 contacts the substrate. When strain is introduced to 3R-MoS_2, researchers have observed a 2–4 order of magnitude increase in the photovoltaic (PV) coefficient in the strained film compared to the unstrained version [26]. This enhancement is primarily attributed to increased asymmetry. Studies on directional photocurrent mapping, depicted in Fig. 6(d), indicate that the net photocurrent generation in the zigzag direction is zero, attributed to the alternating direction of photocurrent within the channel. Conversely, in the armchair direction, a continuous positive photocurrent is observed, which correlates with an elevated BPV coefficient due to strong piezoelectric polarization in that direction for 3R-MoS_2. In the case of 2H-MoS_2, a net zero photocurrent was also observed, which contradicts recent findings regarding layer-number-dependent shift current generation in strained 2H-MoS_2. It has been revealed that shift current generation in strained MoS_2 is only apparent in films with an odd number of layers, as shown in Fig. 6(g) [94]. In contrast, even-numbered layers of MoS_2 possess adjacent layers with opposite dipole moments, which cancel out their polarization, rendering them non-piezoelectric (Fig. 6(h)). This underscores that uniform strain can only facilitate the shift current generation by enhancing the polarization in polar materials.

Research on strain-dependent photocurrent generation has also been conducted in suspended SnP_2Se_6 by C. Xu et al [95]. The strain-induced increase in asymmetry in SnP_2Se_6 is clearly evident in the enhanced second harmonic generation (SHG) signal and Raman shift, as

View Article Online
DOI: 10.1039/D6NH00127K

seen in Fig. 6(i) and (j), which contributes to an increase in the short circuit current of the device (Fig. 6(k)). With its narrow band gap of 1.6 eV, SnP_2Se_6 is particularly promising for photovoltaic applications, as it can produce photocurrent across a broad range of wavelengths. Additionally, it exhibits a higher intrinsic in-plane asymmetry compared to In_2Se_3 and $CuInP_2S_6$, resulting in a remarkable enhancement of the piezo photovoltaic effect under strain application. $GaInSe_3$ also showed a similar phenomenon of strain-induced photocurrent enhancement [96]. In another report, applying mechanical strain to 2H-$MoTe_2$ by placing it on a stretchable PDMS, the 2H to 1T'-$MoTe_2$ transformation is observed, which leads to a reduced band gap and symmetry reduction in $MoTe_2$, thereby resulting in a significant shift in current [97]. Overall, strain allows an extra degree of freedom in the field of BPVE.

The FPVE was first experimentally observed in vdW MoS_2 thin films by placing a portion of the MoS_2 over VO_2, which changes its phase in response to external stimuli, such as temperature (Fig. 7(a)). Therefore, a gradient strain is easily established at the interface region between the phase-changeable substrate and the non-phase-changeable substrate by changing the temperature [98]. A near-perfect light polarization-dependent photocurrent, represented by a sinusoidal curve with a period of 180 degrees, has been observed in centrosymmetric MoS_2. Thus, strained MoS_2 or other centrosymmetric 2D materials could be useful in making a performance self-biased polarized photo detector with high accuracy. Following this work, the flexoelectric engineering of 2D $CuInP_2S_6$ (CIPS) via suspending it over a trench (as shown in Fig. 7(b)) resulted in a 20-fold increase in photocurrent compared to substrate-supported regions, which is also tunable by mechanically changing the force on the suspended region (Fig. 7(c)), confirming the BPVE mechanism. The ultralow dark current and high responsivity also resulted in detectivity as high as 2.679×10^{12} Jones, surpassing ferroelectric-based photodetectors and rivaling commercial silicon photodiodes [99]. DFT simulation on the flat and bent surfaces of the CIPS reveals that the bent surface possesses a symmetric double-well potential, whereas the flat surface has a symmetric double-well potential, as illustrated in Fig. 7(e) and (f). Because of the low-energy metastable state at the stretch surface of bent CIPS, the Cu ion always tries to keep itself at the stretch surface, which generates a Flexoelectric polarization field in the out-of-plane direction. Thus, it creates a potential barrier between the top and bottom, as shown in Fig. 7(g), which facilitates the separation of electron-hole pairs and improves photo detection [25]. Applying a strain gradient in 1T'-$MoTe_2$ by fabricating a simple two-terminal device over a PET substrate and bending the substrate (Fig. 7(h)), a significant improvement in self-biased photocurrent is observed, which proves the simplicity of the Flexo photovoltaic effect. It is further reported that the BPV coefficient has been improved in strained 1T'-$MoTe_2$ compared to the unstained device

View Article Online
DOI: 10.1039/D6NH00127K

(as depicted in Fig. 7(i)), through reduced band gap facilitated by the strain, as illustrated in Fig. 7(j) [91]. FPV is also observed in simple systems, such as keeping VPNS on the nano edge of hBN, as shown in Fig. 7(k), where the nano edge generates a strain gradient in the VPNS and induces the Flexo electric effect (Fig. 7(m)) [100]. Enhanced shift current through FPVE is studied in Bi_2Te_2 and 2H-MoS_2 by inducing a strain gradient through keeping the sample on a curved surface and then making it flat after depositing the film, as well as by keeping the sample on a micro trench, respectively, indicating the diversity of the platform [101,102]. The findings hold promise for practical applications in photo detection, pressure sensing, and beyond, paving the way for innovative device designs. In previous studies, various geometries, such as bending, suspended film, and nano-edge, have been implemented, which may generate different amounts of strain. Although the flexoelectric coefficient is an intrinsic normalization factor of FPVE that dictates the induced polarization per unit strain, polarization is highly non-uniform. The same amount of strain may yield different photocurrents in different geometries, depending on charge-transfer dynamics, polarization distribution, and other factors. Therefore, as a uniform benchmarking factor, the induced current density per unit strain gradient would be important for comparing the performance of the different adopted geometries to improve FPVE.

8. Other various strategies to improve BPVE

Apart from the strain-induced improvement of BPVE, several different strategies are adopted by the researchers, such as edge contact with a semimetal to reduce the contact resistance, introducing defects or disorders to reduce the symmetry of the system, involving the interface of two 2D vdW materials: heterojunction or heterostructure, and twisting the layers with respect to each other [47,103–105]. It is proving the flexibility of the vdW materials in engineering the BPVE. In this section, the mentioned strategies are discussed categorically.

a. Edge-contact semimetal

Using edge contact (EC) on the 3R-MoS_2 channel using Bi semimetal, as shown in Fig. 8(a), substantial enhancements of I_{SC} and V_{OC} compared to top contact (TC) are observed, as presented in Fig. 8(b), because lateral transport of carriers in 3R-MoS_2 is much higher than the vertical transport, thereby facilitating effective collection of carriers as well as Bi generate local strain at the edge which also partially improve the shift current characteristic via reduced symmetry [47]. It also improves the controllability of the device, such as I_{SC}, for the device with TC saturated at a MoS_2 thickness of 15 nm, whereas in the case of EC saturation, it begins at a thickness of 40 nm. In Fig. 8(c), it is clear that in TC, the photocurrent originates from the Schottky barrier, while in EC, the photocurrent is generated from the bulk of the film.

View Article Online
DOI: 10.1039/D6NH00127K

b. Disorder-Induced BPVE

Like any other phenomenon, BPVE is also influenced by defects or disorders. Au-assisted exfoliated $PtSe_2$ generates cluster-like defects, as observable in the Raman shift and STEM-HAADF image in Fig. 8(d) and (e), respectively; these defects induce large photovoltage, which is not detectable in the case of $PtSe_2$ transfer by the normal dry exfoliation method [103]. This phenomenon is the effect of cluster-like defects that induce reduced crystal symmetry. However, Se vacancies could act as asymmetric trigonal scattering sites, where photogenerated electron-hole pairs could react differently, as predicted by first-principles calculations. Two orders of enhancement of the LPGE effect in electron-beam-irradiated defective WSe_2 compared to the pristine one were also reported in the literature. Generated defects reduce the spatial symmetry and increase the spatial separation of e^- and h^+ after generation [106].

The effect of disorders in LPGE is also theoretically predicted in Janus MoSSe; introducing GB significantly reduces the spatial symmetry (C_{3V} to C_1) and results in an enhanced photocurrent, as presented in Fig. 8(f) to (i) [107].

c. Heterojunction and heterostructure

Recently, vdW heterojunctions have been receiving significant attention due to the possibility of symmetry breaking at the interface. Exploiting the low geometric symmetry of the edge-embedded structure, as shown in Fig. 9(a) because of quasi-1D edge states and existence of local strain, of homo or heterostructures such as ReS_2/ReS_2, MoS_2/MoS_2, and WS_2/ReS_2, an improved BPVE effect was also demonstrated in scientific reports, signifying the possibility of applying the heterostructure or heterojunction of vdW materials in the BPVE devices [108]. As shown in Fig. 9(b), the D_{3h} symmetry of the monolayer 2D TMDC can be transformed into three polar groups: C_2, C_{2v}, and Cs, with in-plane polarization. This transformation is achievable by creating a heterostructure with different lattice structure materials. For instance, the MoS_2/BP vdW heterostructure reduces the symmetry from D_{3h} to C_S, leading to a synergistic effect of in-plane and out-of-plane dual-polarization (Fig. 8(c)), which supports ultrafast and high-efficiency BPVE [104].

Furthermore, the concept of a heterojunction of highly light-absorbing 2D-$MoSe_2$ and strong IP ferroelectric $NbOI_2$, which generates strong BPVE, is also demonstrated experimentally (Fig. 9(f)) [109]. The ultra-fast hole transfer from $MoSe_2$ to $NbOI_2$ and electron transfer in the opposite direction, with time constants of 0.4 and 3.8 ps, respectively, enables substantial exciton generation and dissociation at the interface. Additionally, the IP ferroelectricity-induced dc electric field and built-in electric field at the junction result in

View Article Online
DOI: 10.1039/D6NH00127K

excellent photoresponsivity. Application of a DC poling voltage just before photodetection enhances the strength of polarization. It improves the responsivity, allowing for control of the photocurrent direction in this type of system, as depicted in Fig. 9(h). Improved performance of the $MoSe_2/WSe_2$ heterojunction device is also demonstrated by inducing FPVE and/or Peizo-PVE [110].BPVE generation via the symmetry breaking at the interface of the WS_2/CrOCl heterostructure device has also been reported in the literature [111]. Significant enhancement of BPVE by symmetry engineering in Black – Phosphorus and Blue – Phosphorus heterojunction compared to Blue – Phosphorus homo junction has also been predicted through theoretical calculation [112]. The shift current Graphene/BN superlattice structure was also theoretically predicted due to the reduced symmetry of the system to C_{2v} [113]. Overall, through the construction of vdW heterostructures, the effective manipulation of the system's symmetry and improvement of BPVE are feasible.

d. Twisted vdW Materials in BPVE

Integrating a vdW layer at a specific twist angle relative to another layer creates a moiré superlattice, as demonstrated in double-layer twisted MoS_2 (Fig. 9(i)). This engineering approach leads to fascinating physical phenomena by reconstructing electronic bands and generating quantum geometric properties. These changes can alter the Berry curvature of the bands and produce new symmetries. Recently, the shift current generation has been reported in twisted MoS_2, as shown in Fig. 9(k), which exhibits polarization-sensitive photocurrent at 780 nm [105]. This is facilitated by phonon-assisted transitions that mediate a nonzero displacement of electron and hole wave packets. In twisted bilayer graphene, a shift has also been predicted in a recent report [114]. Therefore, twisting the vdW material could generate a new avenue for exploring BPVE. In another recent computational study on the WSe_2/WS_2 moiré superlattice, a groundbreaking phenomenon, a shift current vortex crystal, was observed. Periodic 2D arrays of moiré-scale current vortices can generate remarkably intense magnetic fields under the application of light. Even the shift current vortices, shape, chirality, and intensity are tunable by the frequency, polarization, and intensity of the incident light [115]. Due to the twisted screw structure of spiral WS_2, it is noncentrosymmetric and exhibits strong SHG; however, no investigation of BPVE on spiral WS_2 has been conducted yet [116].

9. Key challenges in the performance of BPVE in 2D vdW Materials

Although, in the reported publications, EQE for the devices is not measured at a standard solar AM 1.5G power density (~100 mW cm^{-2}), also no distributed light or EQE distribution over wavelength has been considered during measurement in most of the earlier publications,

View Article Online
DOI: 10.1039/D6NH00127K

it is very difficult to compare the device to device; however, if we consider that EQE has very slow variability with optical power, the highest reported EQE in converting photon to electrical charge is about 30% at high intensity irradiation of light of wavelength 400 nm using distorted $MoTe_2$ (see Supplementary Table S1) which is far below the traditional pn-junction photovoltaics. The power conversion efficiency of the 2D vdW-based BPVE devices is also very low, typically <5% in most studies. Several factors most likely influence the low efficiency, which will be discussed categorically.

Intrinsic conductivity limits V_{OC}: From the comparison of the different 2D vdW-based devices shown in Fig. 10(c) (Reported by Qiao et al. [47]), it is evident that J_{SC} is not the primary limiting factor. Substantial J_{SC} values have been achieved across various device structures, in some cases comparable to those of standard commercial *pn* junction solar cells. These results indicate that the primary performance limitation arises from the inefficient V_{OC} (as presented in Supplementary Table S1 for different material systems), especially in devices with a lateral configuration (in-plane), where performance is dominated by the shift current mechanism. Indeed, V_{OC} in BPVE devices is not limited by the band gap, but rather by other factors, such as the intrinsic conductivity of the sample. V_{OC} is a status where the balance of photon-induced shift current and static electric field (generated by external electric field) induces drift current. In an ideal scenario, without considering contact resistance, this can be represented by the simple circuit diagram in Fig. 10(a). V_{OC} is therefore inversely proportional to the intrinsic conductivity σ of the absorber material, due to photogenerated carriers, and to the distance between contacts d, as proposed by Pusch et al. [30]. Essentially, V_{OC} is proportional to the resistance of the absorber layer, as reported in various articles related to shift current. Thus, with a high J_{SC}, the enhanced photoconductivity of the active material will essentially counterbalance the V_{OC}. Therefore, semiconductors with low conductivity can generate high V_{OC}; however, this may also cause reduced I_{SC} by diminishing ballistic transport after the electric field shifts the carrier.

Linear output characteristic of shift current device fixed fill factor at 25%: As the built-in potential does not exist in the shift current generating device, like a pn junction, the shift current generating device acts as a current source where the device current linearly decreases with increasing voltage due to linear drift of the carrier in the bulk material. Essentially, the output characteristics of shift-current-dominated BPVE devices are linear, with the maximum power point at half of V_{OC} and half of I_{SC}, as shown in Fig. 10(b), resulting in only a fill factor of 25%, a serious intrinsic limitation. The DEP field-induced BPVE is not immune to the Shockley-

View Article Online
DOI: 10.1039/D6NH00127K

Queisser limit, as polarization introduces band bending at the interfaces, and the effect is essentially energy barrier-related. V_{OC} in DEP-induced BPV devices is higher than that in shift current-driven devices, and their fill factor is not limited to 25%.

Limited photon absorption by the thin 2D layer limits EQE: Inefficient photon absorption at ultra-thin 2D layers and recombination of charge carriers at the electrode region can significantly limit performance, which is clearly visible in the low EQE of the devices. Using a thick layer of photon absorption could be improved; however, the symmetry and light absorption capability abruptly change in 2D vdW materials, such as 2H-MoS_2, which transforms into an indirect band gap material at thicknesses higher than ~10 layers. Instead of using a thick layer that may not yield any improvement, the previously proven concept of monolithic integration of 2D material-based devices could be investigated [117], which will convert it into a photon that will be transmitted through the prior device. Therefore, monolithic integration could be a feasible route in improving device efficiency.

Moreover, contact resistance is also a limiting factor for reduced J_{SC}. It can be reduced by electrode engineering using semimetal contacts, such as Graphene, Bi, or other engineering approaches, as experimentally evident in the case of Bi edge contact on 3R-MoS_2.

Furthermore, for energy-related applications, the Earth's abundance of elements should be considered while evaluating the actual benefit of the device in real-world applications. From Fig. 10(d), elements such as Re, Te, and Se are extremely rare on Earth [118], and their mining is proportionally energy-intensive and costly, which inherently generates a negative environmental impact. Indium is also considered scarce when dealing with the Si *pn* junction devices. The elements Mo, W, Ge, Sn, and S are relatively abundant, and further exploration of BPVE devices for solar energy conversion will be beneficial in reducing the carbon footprint on Earth.

Likewise, scalability is a relevant issue for 2D vdW material-based BPVE, as large-scale synthesis of these 2D materials remains challenging. Although in the past few years the 2H phase of TMDCs has been extensively investigated to enable large-scale synthesis, controlling thickness, grain boundaries, defects, and uniformity still needs to be addressed. The strong BPVE candidates, such as the 3R phase of TMD, Janus TMDC, and mono chalcogenides, remain significantly less mature than the 2H phase TMDC [119]. Heterostructures like NbOI2 and TMDC require a multi-step growth process, further limiting scalability. Therefore, for particle device applications, material selection must balance earth-abundant materials with manufacturability to achieve sustainable, realistic commercialization.

View Article Online
DOI: 10.1039/D6NH00127K

10. Conclusion and Future Outlook

2D vdW materials, due to their extraordinary features such as tunable band gaps, diverse crystal structures, robust mechanical strength, and the ability to retain clean interfaces even in ultra-thin atomic layers, among others, occupy a highly valuable position in the research of electronics and optoelectronics. To date, substantial investigation has been carried out on BPVE in 2D vdW materials; however, the experimental efficiency of the device lacks the minimal efficiency required for practical solar energy conversion devices.

Large-scale synthesis of vdW materials remains under investigation, posing another challenge for practical device applications. Considering the sustainable development of energy-related materials, Mo, W, and S are in suitable positions on the Earth-abundance scale. Also, the large-scale fabrication of 2H-MoS_2 and WS_2 is quite successful at the laboratory scale; however, they are not strong candidates for BPVE because they lack intrinsic polarization. In contrast, their 3R phase exhibits intrinsic polarization and is a strong candidate for BPVE. Although there are few reports in the literature on the large-scale synthesis of the 3R phase of WS_2 and MoS_2, further investigation into optimizing their scalability and subsequent studies on the material's performance in BPVE will be highly beneficial.

The weak light absorption of the ultra-thin 2D vdW layer can be efficiently addressed by utilizing a monolithic cascade device architecture, which has the potential to generate higher current density by absorbing the unutilized light in the subsequent layer. The 25% Fill factor of the shift-current-dominated devices could be addressed by employing a carrier-selective asymmetric contact, which introduces nonlinearity in carrier conduction and might reshape the device's output characteristics. However, no theoretical or experimental evidence is yet available; intuitively, there might be an interplay between the artificial nonlinearity and the barrier-independent shift-current mechanism to realize an elastic route to leverage the band-gap limitation.

2D vdW Weyl semimetals are very sensitive to weak microwave photons, and their polarization-selective response adds an extra dimension of secure communication in military applications. The bias-free operation and ultrathin dimension, which even yield performance comparable to that of commercial microwave detectors, will be attractive for low-cost commercial microwave detectors.

Furthermore, investigating different strategies, such as edge contact, twisted 2D layers, heterojunctions with various materials, and defect tuning, among others, will enrich the

View Article Online
DOI: 10.1039/D6NH00127K

fundamental science of the BPVE of vdW materials. Polarized photo detectors also have tremendous importance in biomedical analysis, secure communication, surface identification, and many other applications. DEP field-induced BPVE in 2D vdW materials could be especially attractive for making self-biased, energy-efficient, highly dense photodetector arrays, given their vertical configuration. 2D vdW BPVE devices are compatible with on-chip integration and complex circuitry. By carefully leveraging the self-bias photocurrent, it is possible to design an optical bionic vision system that operates at very low power, and polarized photodetection will add a new feature to smart devices. Designing 2D vdW-based BPVE devices tailored for these applications could be a promising pathway to harness this phenomenon in energy-efficient, advanced next-generation optoelectronic devices.

Notes

The authors declare no competing financial interest.

Acknowledgments

This research was supported by the National Research Foundation of Korea (NRF) and the Ministry of Education, Korea.

View Article Online
DOI: 10.1039/D6NH00127K

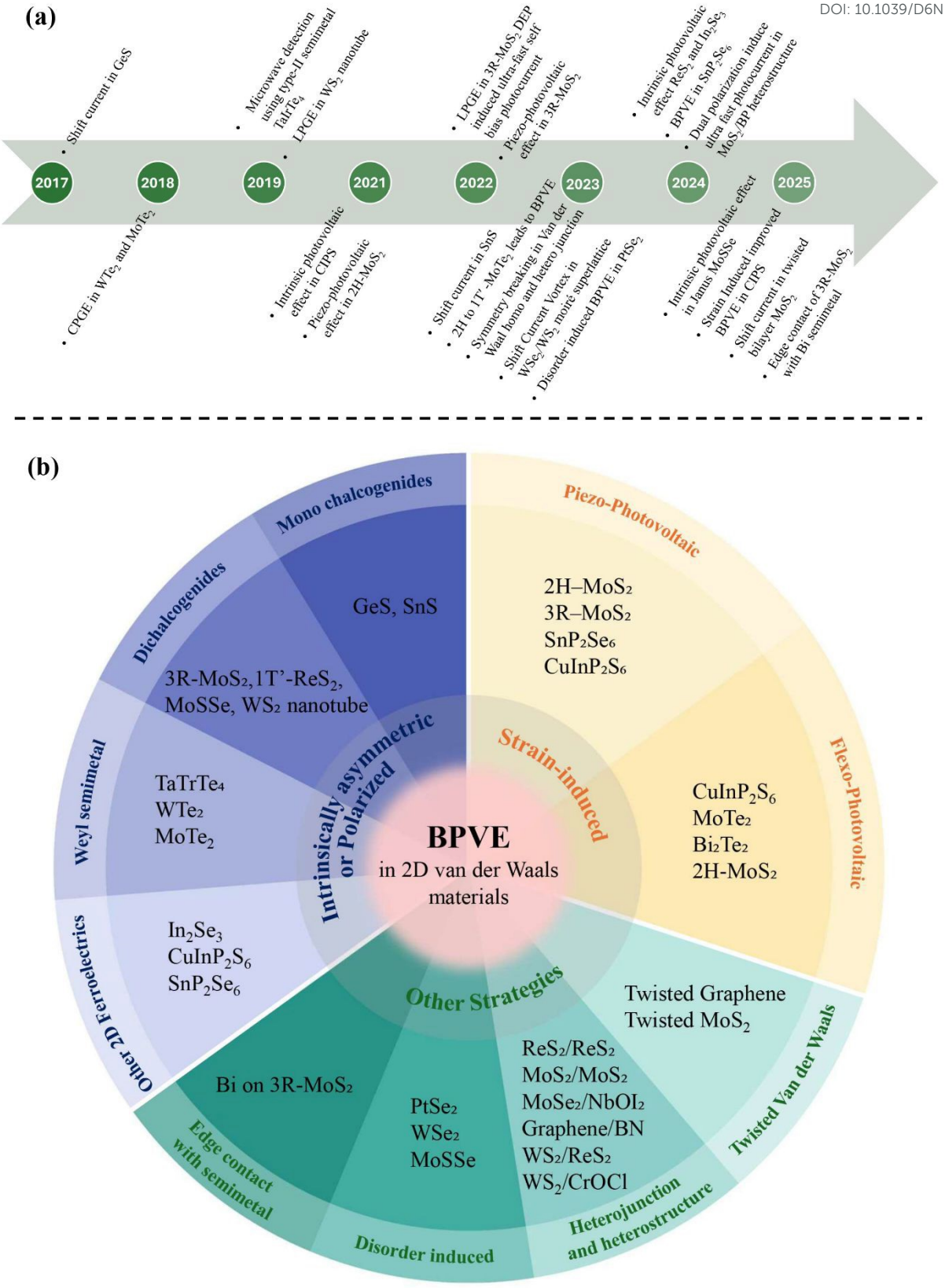

Fig. 1 (a) Historical evolution of BPVE in 2D vdW materials. (b) schematic representation of the BPVE observed in different materials and related techniques.

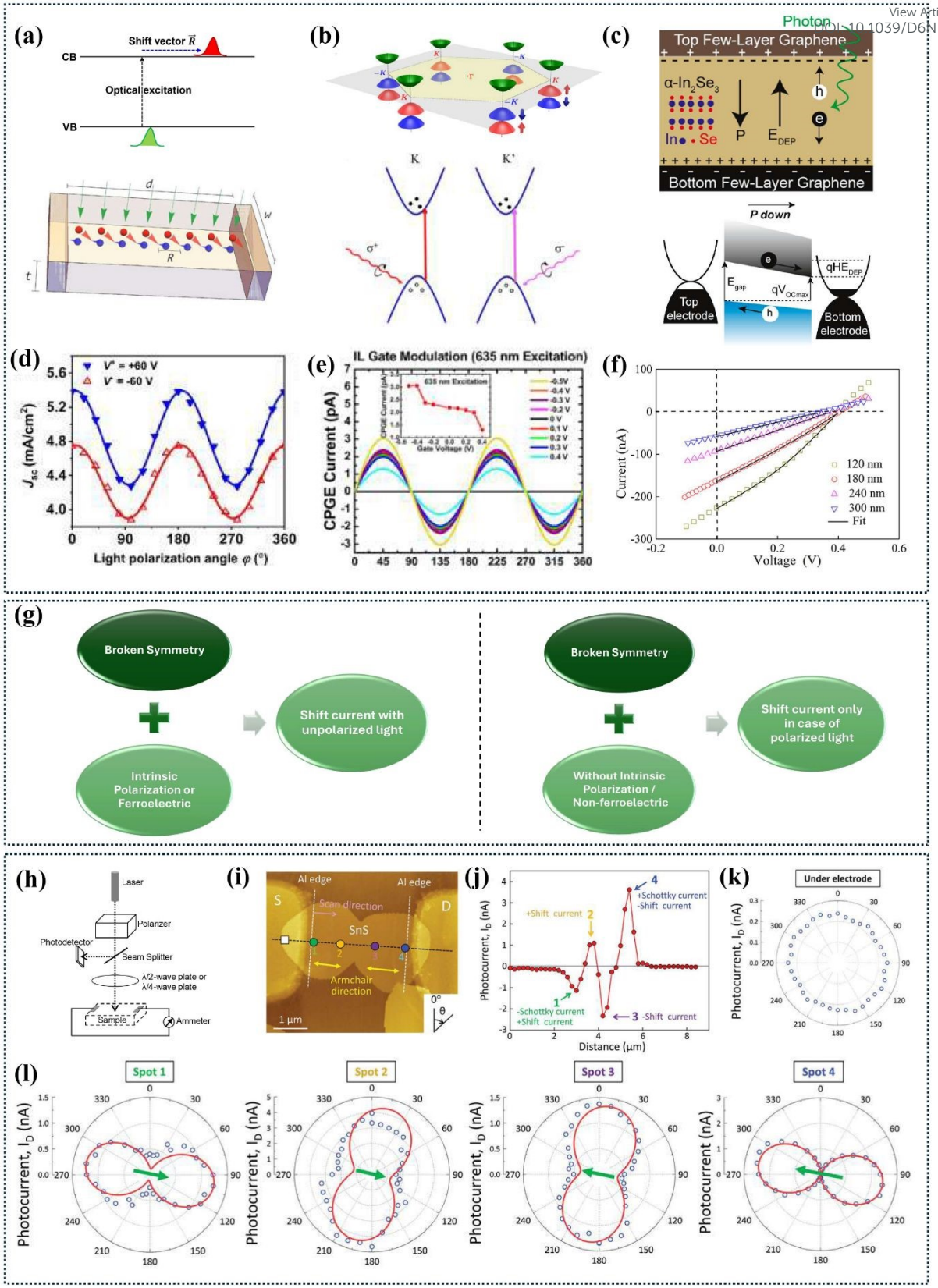

Fig. 2 ***Mechanism and characterization of BPVE.*** (a) On top: schematic diagram of shift current generation across the band gap, and on bottom: average shift of the charges (electrons and holes) per absorption event of the incoming light (green arrows) is denoted as *R*. (b) On top: schematic drawing of the band structure at the band edges located at the K points, and on bottom: schematics of the process of inter band transition circular polarized excitation, carriers at the K (K') valley can only be

View Article Online
DOI: 10.1039/D6NH00127K

excited by LCP/RCP light which is represented by the red (pink) curves. (c) On top: schematic diagram of the device architecture and DEP field-induced FPVE in In_2Se_3 device, and on bottom: band diagram of the In_2Se_3/Graphene heterostructure. (d) Dependence of the J_{sc} on the light polarization angle φ, in h-$LuMnO_3$ ferroelectric crystal. (e) CPGE current as a function of the applied gate voltage. (f) DEP field induced BPVE in the $Pb(Zr_{0.2}Ti_{0.8})O_3$ films. (g) Condition of the shift current generation with polarized and unpolarized light. (h) A simple schematic diagram of a polarization-dependent photocurrent measurement setup. (i) AFM topographic image of an SnS device with two-linked crystals measured before the application of *h*-BN encapsulation and Al film, (j) Unbiased photocurrent obtained from the drain electrode along the black dotted line shown in (i), (k) Angular-dependent photocurrent induced by linearly polarized light measured at the electrode region covered by Al film, whose position is indicated by the white rectangle in (i), and (l) Angular-dependent photocurrents induced by linearly polarized light measured at spots 1–4. Green arrow is the predicted spontaneous polarization direction.

Panel bottom (a) reproduced from the Ref. [30], copyright 2023 American Physical Society; Panel top (b) reproduced from the Ref. [41], copyright 2012 American Physical Society; Panels bottom (b) and (e) reproduce from ref. [6], copyright 2017 American Physical Society. Panel (c) reproduced from the Ref. [24], copyright 2024 American Chemical Society; Panel (d) reproduced from the Ref. [33], copyright 2022 AIP Publishing; Panel (f) reproduced from the Ref. [45], copyright 2019 Springer Nature; Panels (i) to (l) reproduced from the Ref. [48], copyright 2023 Wiley-VCH GmbH.

View Article Online
DOI: 10.1039/D5NH00127K

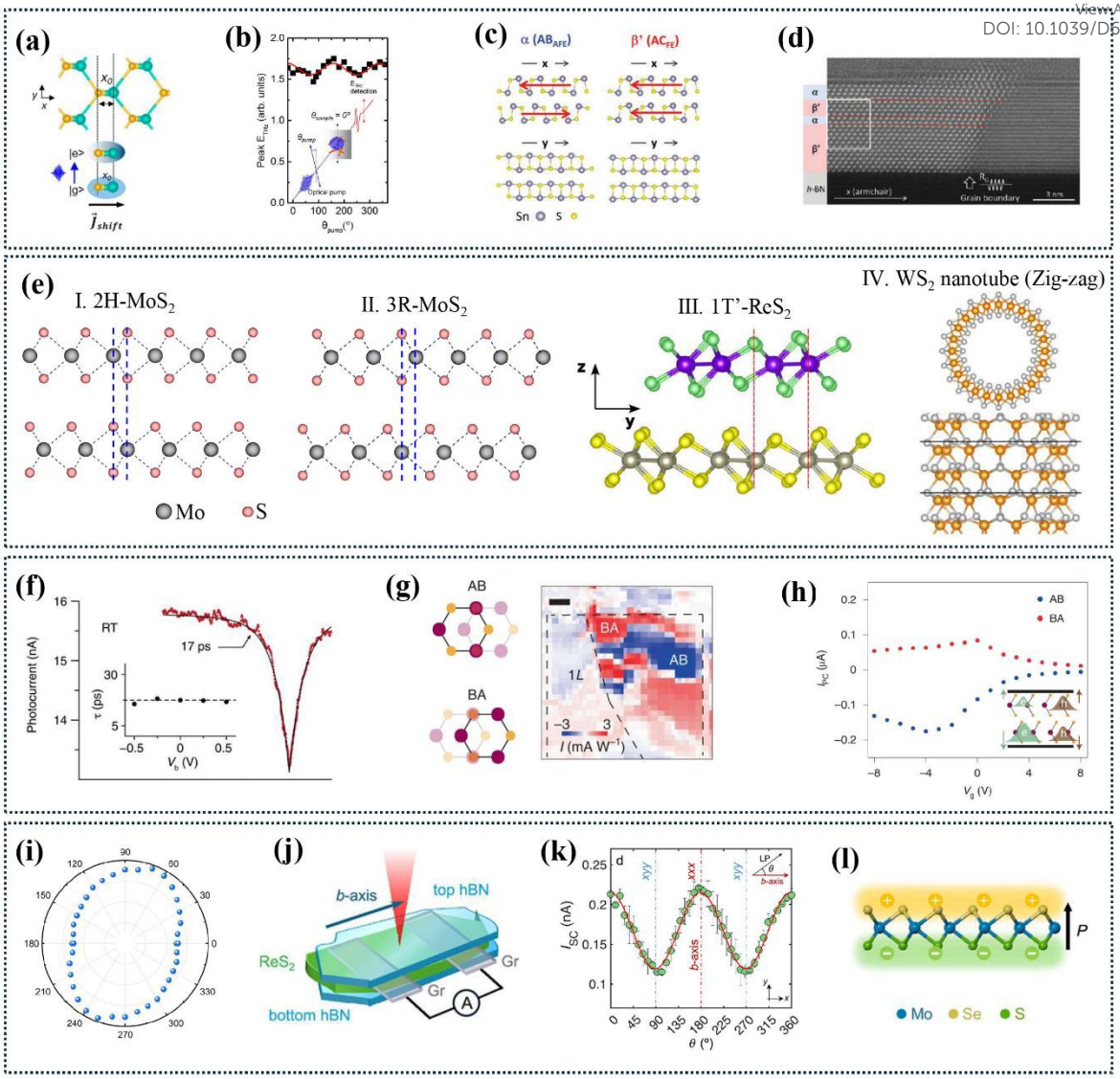

Fig. 3 ***Transition Metal chalcogenides.*** (a) Top view of the structure of GeS monolayer exhibiting spontaneous distortion in the x direction and schematic depiction of an in-plane shift current due to an ultrafast transfer of electron density along the S−Ge bond; (b) THz pulse peak as a function of linear polarization of the pump.. (c) The schematic illustrations of crystal structures in the α and β' phases of SnS in x (armchair) and y (zigzag) direction; (d) The transition area between the β' and α phases of SnS. (e) Side view of different TMDC systems, I. bilayer 2H-MoS_2, II. bilayer 3R-MoS_2, III. bilayer 1T'-ReS_2, IV. WS_2 nanotube rolled in zig-zag direction, bottom showing broken mirror symmetry in the z-direction. (f) Autocorrelation signals of the BL region of 3R-MoS_2 measured at RT. The dotted lines are from experimental measurements, and the black lines are exponential fittings to extract the time constants. (g) Schematic of two possible stacking domains (AB and BA) of a 3R bilayer MoS_2 (left); The top layer (solid) shifts towards the left (AB) and right (BA) relative to the bottom layer (translucent). A scanning PC map of the device demonstrates that the positive and negative photoresponse areas correspond to the AB and BA domains; (h) Gate voltage-dependent PC in the AB and BA domains. The inset shows a schematic of the charge transfer between 3R-MoS_2 and graphene. Electrons are partially layer polarized, whereas holes are equally distributed between the two layers. (i) Polar plot of I_{sc} with respect to the polarization of the pump laser measured from the tetralayer ReS_2

View Article Online
DOI: 10.1039/D6NH00127K

vertical PV device. (j) Simplified three-dimensional device scheme of Graphene contacted ReS_2 showing the different vdW layers composing the system. (k) Angular dependence of the short-circuit current measured along the b-axis of ReS_2 as a function of the linear polarization of the incoming light. (l) Structure of the Janus MoSSe monolayer with intrinsic polarization (P).

Panels (a) and (b) reproduced from the Ref. [20], copyright 2017 American Chemical Society; Panels (c) and (d) reproduced from the Ref. [48]; copyright 2023 Wiley-VCH GmbH; Panels (g) and (h) reproduced from the Ref. [21], copyright 2022 Springer Nature; Panels (e)-III, (j), and (k) reproduced from the Ref. [22], copyright 2024 American Chemical Society; Panel (e)-IV reproduced from the Ref. [66], copyright 2022 Springer Nature; Panel (f) reproduced from the Ref. [7], copyright 2022 The American Association for the Advancement of Science; Panel (i) reproduced from the Ref. [64], copyright 2024 The Royal Society of Chemistry; Panel (l) reproduced from the Ref. [68], copyright 2025 Springer Nature.

View Article Online
DOI: 10.1039/D6NH00127K

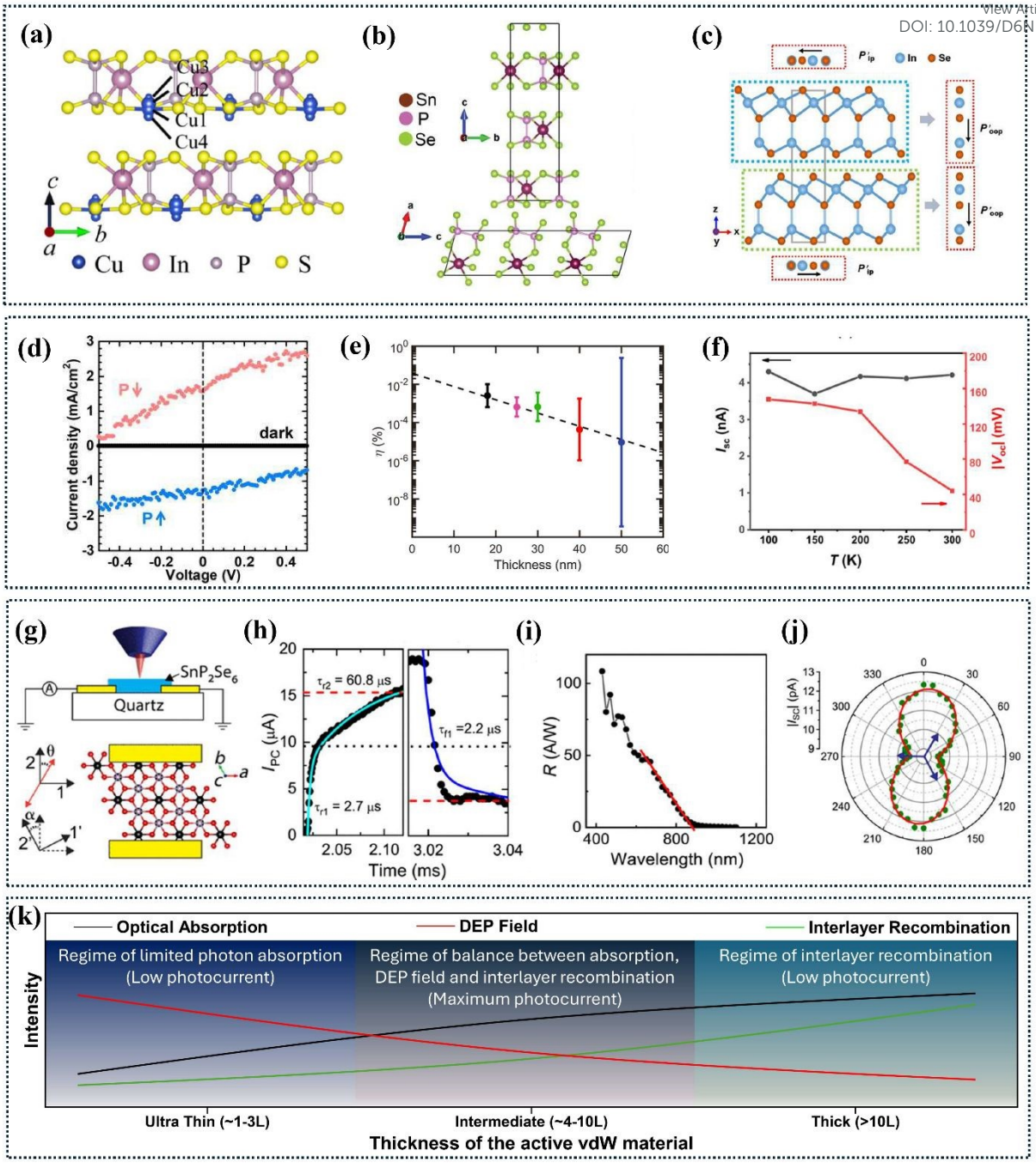

Fig. 4 ***Post-transition metal-based vdW ferroelectric.*** (a), (b), and (c) Side view of CIPS, SnP_2Se_6, and In_2Se_3 crystal structure demonstrating the position of different atoms which induce spontaneous polarization, respectively. (d) J–V characteristics of α-In_2Se_3 along the out-of-plane direction under the conditions of dark and light illumination, red and blue plots correspond to the downward and upward direction of spontaneous electric polarization, respectively; (e) efficiency vs thickness of In_2Se_3 vertical device; (f) Temperature dependence of short circuit current I_{sc} (dark circles) and open circuit voltage V_{oc} (red squares) for vertical In_2Se_3 device. (g) top: Side-view schematic of a bottom-contacted SnP_2Se_6 device on a quartz substrate under photoexcitation; bottom: top-view schematic of the SnP_2Se_6 device; (h) transient photocurrent in SnP_2Se_6 device demonstrating μs response; (i) Responsivity of a SnP_2Se_6 phototransistor at $V_d = -1$ V and $V_G = 0$ V as a function of wavelength; (j)

Angle-resolved I_{sc} of SnP_2Se_6 device; (k) Qualitative phase diagram of thickness-dependent BPVE in 2D vdW materials.

View Article Online
DOI: 10.1039/D6NH00127K

Panel (a) reproduced from the Ref. [23], copyright 2024 American Physical Society; Panel (b) reproduced from Ref. [71], copyright 2025 Wiley-VCH GmbH; Panels (c) and (f) reproduced from Ref. [46], copyright 2025 The Royal Society of Chemistry; Panel (d) reproduced from Ref. [72], copyright 2024 AIP Publishing; Panel (e) reproduced from Ref. [24], copyright 2024 American Chemical Society; Panels (g) to (j) reproduced from Ref. [49], copyright 2024 The American Association for the Advancement of Science.

View Article Online
DOI: 10.1039/D6NH00127K

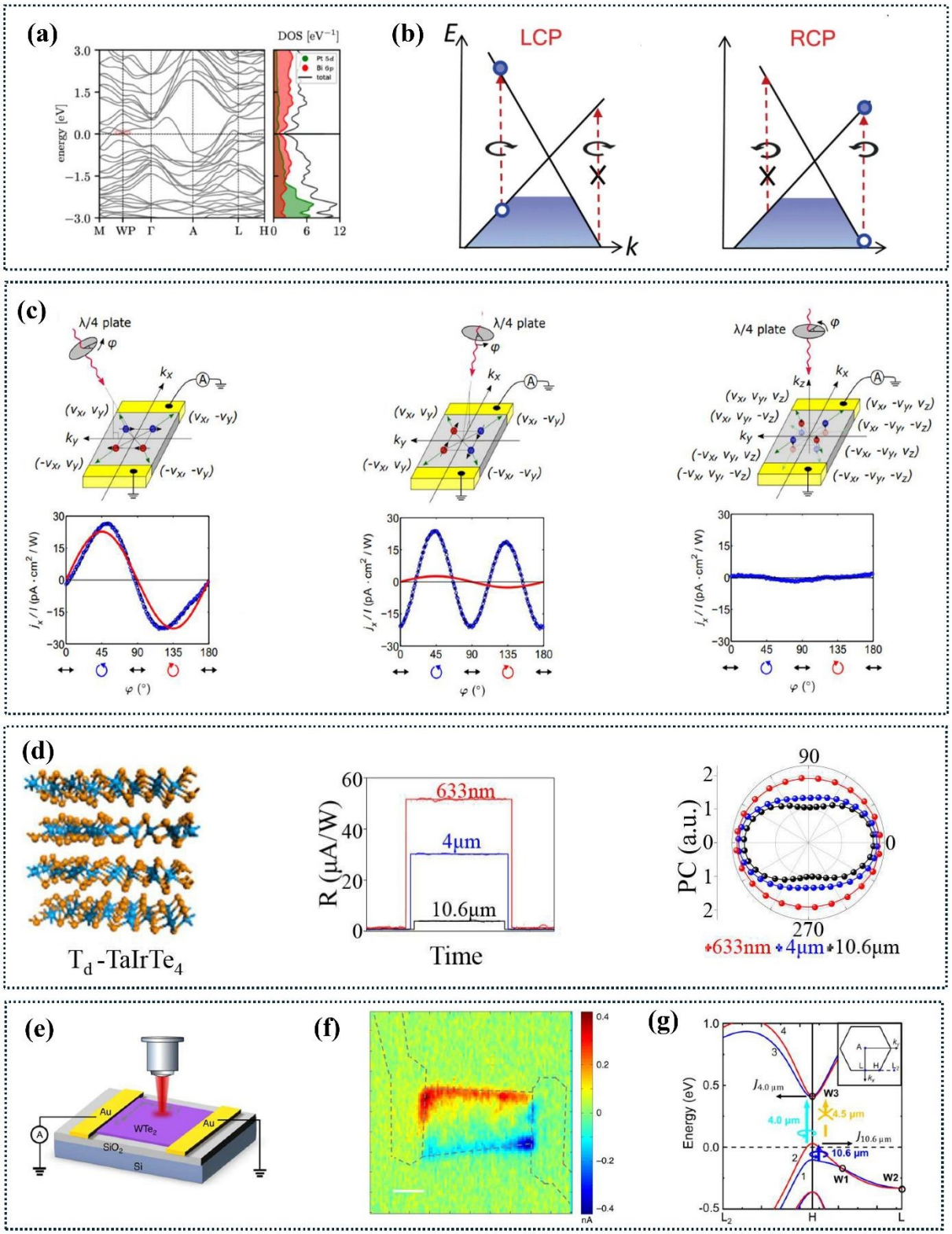

Fig. 5 ***Weyl semimetal.*** (a) Full-relativistic GGA band structure of bulk $PtBi_2$ showing a Weyl node. (b) Chirality selection rule: Right-handed circularly polarized (RCP) light along $+\hat{k}$ excites the $+k_z$ side of the $\chi = +1$ Weyl node but the $+k_z$ side of the $\chi = -1$ Weyl node. Chirality selection rule is independent of the tilt of the WFs; (c) Light obliquely incident in the *x*-*z* plane at an angle of 40° and normal incident, and corresponding generated photocurrent with changing polarization direction. (d)

View Article Online
DOI: 10.1039/D6NH00127K

On left: Crystal structures of $TaIrTe_4$ in the T_d phase; On middle: broadband photo responses. On right: Anisotropic PC response for the linear polarized excitation at 633 nm, 4 μm, and 10.6 μm. (e) Schematic diagram of scanning photocurrent measurement of a WTe_2 field effect device; (f) scanning photocurrent response of a typical 6-nm thick WTe_2 device demonstrating edge photocurrent response in WTe_2; (g) The band diagram near the H point of Te considering spin-orbit interaction. The blue, cyan, and yellow arrows denote transitions induced by 10.6 μm, 4.0-μm, and 4.5-μm excitations, respectively. W1, W2, and W3 mark three Weyl nodes near H point. The energy bands forming W1 and W3 are marked 1–4. The inset shows the Brillouin zone with L, H, and L_2 points.

Panel (a) reproduced from the Ref. [75], copyright 2024 American Physical Society; Panels (b) reproduced from the Ref. [78], copyright 2021 Springer Nature; Panel (c) reproduced from the Ref. [86], copyright 2018 American Physical Society; Panel (d) reproduced from the Ref. [81], copyright 2024 American Chemical Society; Panels (e) and (f) reproduced from the Ref. [88], copyright 2019 Springer Nature; Panel (g) reproduced from the Ref. [89], copyright 2019 Springer Nature.

View Article Online
DOI: 10.1039/D6NH00127K

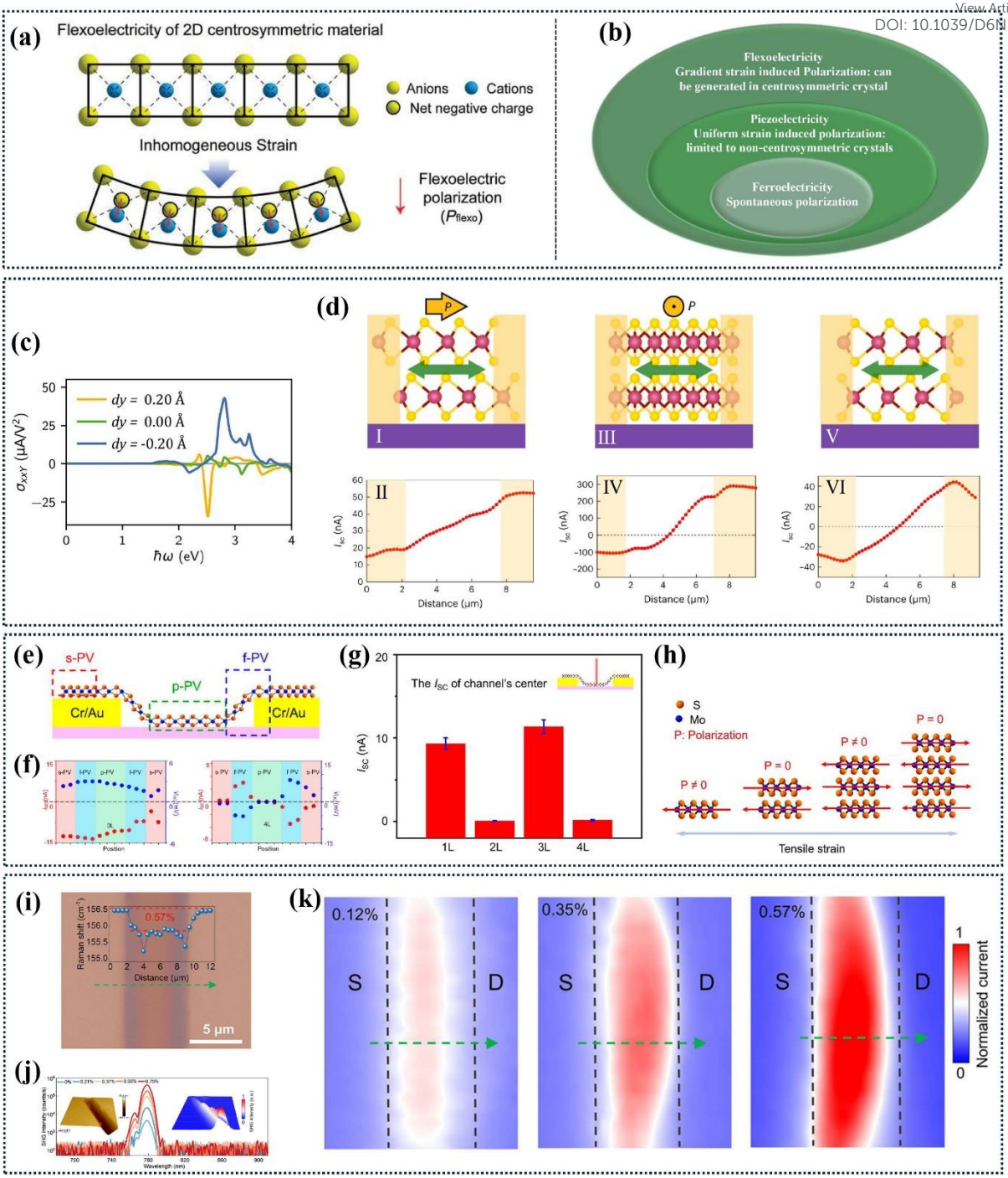

Fig. 6 Strain induces BPVE generation. (a) Schematic diagram of inhomogeneous strain-induced flexoelectric polarization in 2D centrosymmetric crystal. (b) Ven diagram of ferroelectricity, piezoelectricity, and flexoelectricity. (c) Theoretically calculated σ_{XXY} component of the MoS_2 shift current tensor coefficient with Mo displaced at dy = 0.2 Å and dy = –0.2 Å. (d) Device schematic, image, and corresponding photocurrent distribution for 3R-MoS_2 strained along the armchair direction I and II, 3R-MoS_2 strained along the zigzag direction III and IV, and 2H-MoS_2 strained along the armchair direction V and VI. (e) The schematic diagram of the three PV mechanisms present in the strained monolayer 1H-MoS_2 device includes the flexo-photovoltaic (f-PV) effect, piezo-photovoltaic (p-PV) effect, and Schottky-induced photovoltaic (s-PV) effect; (f) Spatial distribution of I_{SC} and V_{OC} on the strained MoS_2 devices with 3L on the left and with 4L on the right; (g) Layer-dependent I_{SC} of strained MoS_2; (h) Mechanism of the p-PV effect. (i) Optical microscopy (OM) image of the uniformly strained SnP_2Se_6. The inset shows the evolution of the Raman shift along the green dashed

View Article Online
DOI: 10.1039/D6NH00127K

line; (j) SHG spectra of SnP_2Se_6 crystals under varying strain states. The inset shows the AFM topography image (left) and the corresponding SHG intensity mapping (right) of the same sample transferred onto a prefabricated trench; (k) Zero-bias photocurrent mapping of the strained devices under different strain levels (The vertical black dotted lines represent the electrode edges).

Panel (a) reproduced from the Ref. [92], copyright 2015 Springer Nature; Panel (c) reproduced from the Ref. [65], copyright 2021 American Chemical Society; Panels (d) reproduced from the Ref. [26], copyright 2023 Springer Nature; Panels (e) to (h) reproduced from the Ref. [94], copyright 2024 American Chemical Society; Panels (i) to (k) reproduced from the Ref. [95], copyright 2024 American Chemical Society.

View Article Online
DOI: 10.1039/D0NH00127K

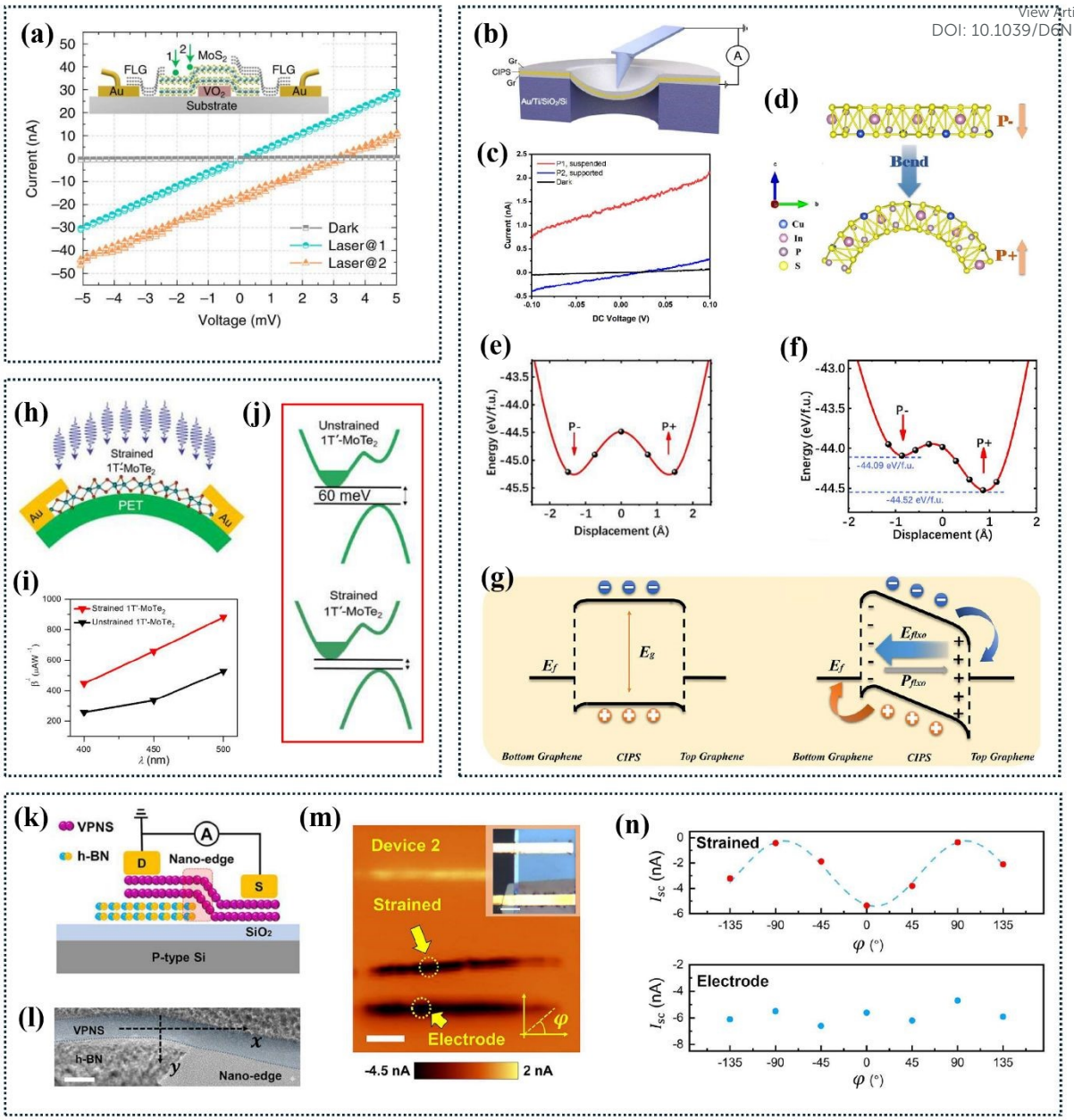

Fig. 7 ***Gradient strain-induced Flexoelectric effect.*** (a) Current–voltage curves of the flexoelectric engineered MoS_2 by phase change VO_2 under laser (532 nm) illumination at spot 1 (Laser@1) and 2 (Laser@2) and without illumination (Dark). The inset shows a schematic of the cross-sectional view of the device. (b) Schematic of the device configuration of flexoelectric engineered suspended CIPS in the vertical direction using top and bottom contact with Graphene; (c) I–V curves measured on suspended (red) and substrate-supported (blue) regions; (d) The schematic crystalline structure of the flat and bent CIPS; (e) and (f) The calculated potential energy profiles (PEP) for flat and bent CIPS, respectively; (g) The energy band diagram of flat CIPS (on left) and bent CIPS (on right) in the initial state at zero bias. The bound charges are identified by the symbols "+" and "–". (h) Schematic representation of strained 1T′-$MoTe_2$ on the flexible polyimide substrate; (i) BPVE coefficient for strained and unstrained 1T′-$MoTe_2$ nanoflakes as a function of incident light wavelength; **(j)** schematic band structure of unstrained and strained 1T′-$MoTe_2$, showing the energy separation. (k) Schematic images of the fabricated nanodevice featuring VPNS and h-BN nanoedge; (l) Scanning transmission

View Article Online
DOI: 10.1039/D6NH00127K

electron microscopy (STEM) results of VPNS device, demonstrating strain at the nano edge; (m) Short-circuit photocurrent map of the strained VPNS device demonstrating significant photocurrent generation at the strained region compared to the unstrained region; (n) Dependence of the absolute value of the FPV photocurrent for strained VPNS on the direction of polarization at the strained region (on top) and at the electrode (on bottom), proving the shift current mechanism.

Panel (a) reproduced from the Ref. [98], copyright 2021 Springer Nature; Panels (b) and (c) reproduced from the Ref. [99], copyright 2024 American Chemical Society; Panels (d) to (g) reproduced from the Ref. [25], copyright 2024 American Chemical Society; Panels (h) to (j) reproduced from the Ref. [91], copyright 2023 American Chemical Society; Panels (k) to (n) reproduced from the Ref. [100], copyright 2024 American Chemical Society.

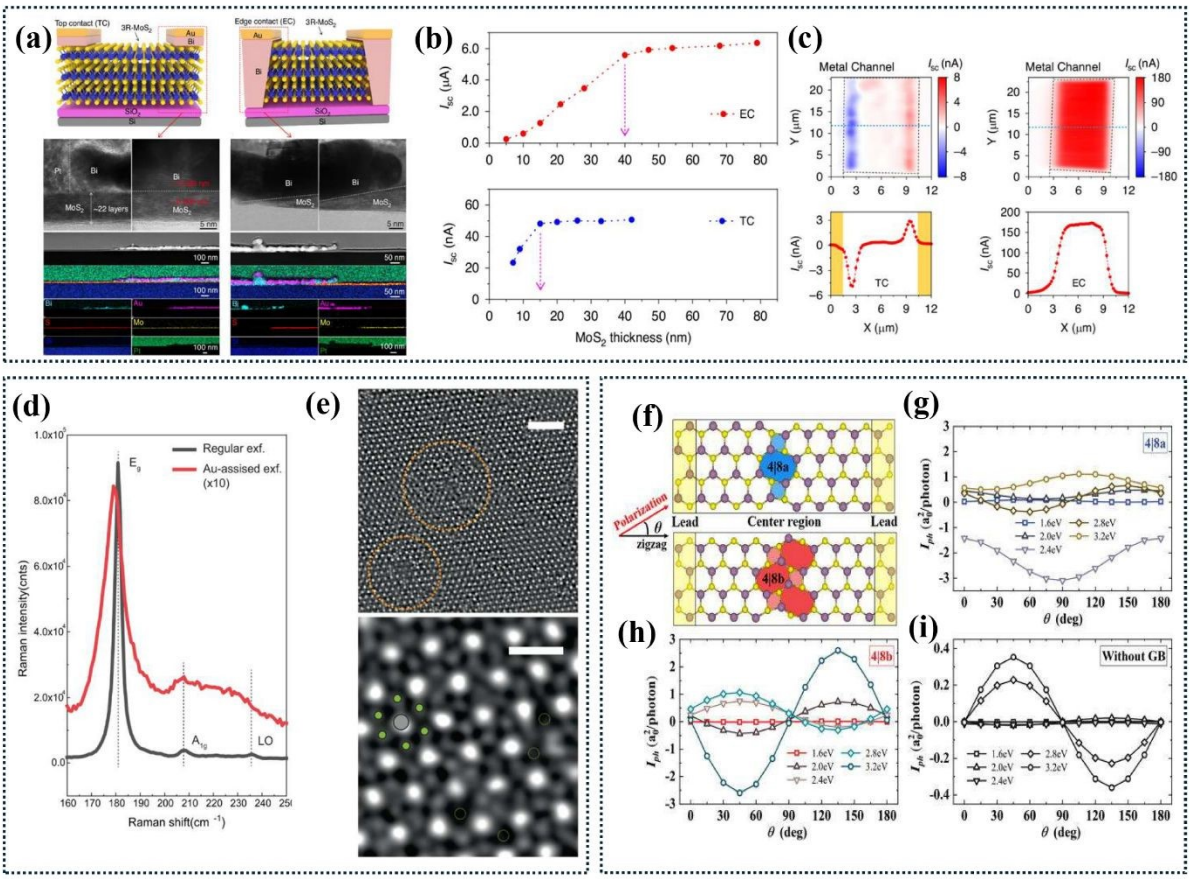

Fig. 8 ***Edge-contact and defect engineering.*** (a) On top left and right, schematic illustrations of the 3R-MoS_2 with semimetal Bi TC & EC devices, respectively, and bottom left and right, cross sectional HRTEM images and STEM-EDS elemental mappings in the right electrode region of the TC device, and the left electrode region of the EC device, respectively; (b) and (c) Short circuit current and photovoltage for both the TC and EC devices. The spatial photocurrent mapping for the TC and EC devices and the illumination position dependences of I_{SC} corresponding to the marked dotted light-blue lines. (d) Raman spectra of monolayer $PtSe_2$ samples produced by regular exfoliation (black line) and Au-assisted exfoliation (red line); (e) On top, STEM-HAADF image of a bilayer $PtSe_2$ from Au-assisted exfoliation. The cluster-like defects are highlighted by orange dashed circles, and at the bottom, a STEM-HAADF image with a small field of view is shown. The green and gray dots

represent Se and Pt atoms, respectively, and Se vacancies, displayed as dotted yellow circles. (f) Different types of grain boundaries in Janus MoSSe; Polarization-dependent photocurrent of (g) 4j8a GB, (h) 4j8b GB, and (i) without-GB monolayer excited.

View Article Online
DOI: 10.1039/D6NH00127K

Panels (a) to (c) reproduced from the Ref. [47], copyright 2025 Springer Nature; Panels (d) and (e) reproduced from the Ref. [103], copyright 2023 Springer Nature; Panels (f) to (i) reproduced from the Ref. [107], copyright 2023 AIP Publishing house.

View Article Online
DOI: 10.1039/D6NH00127K

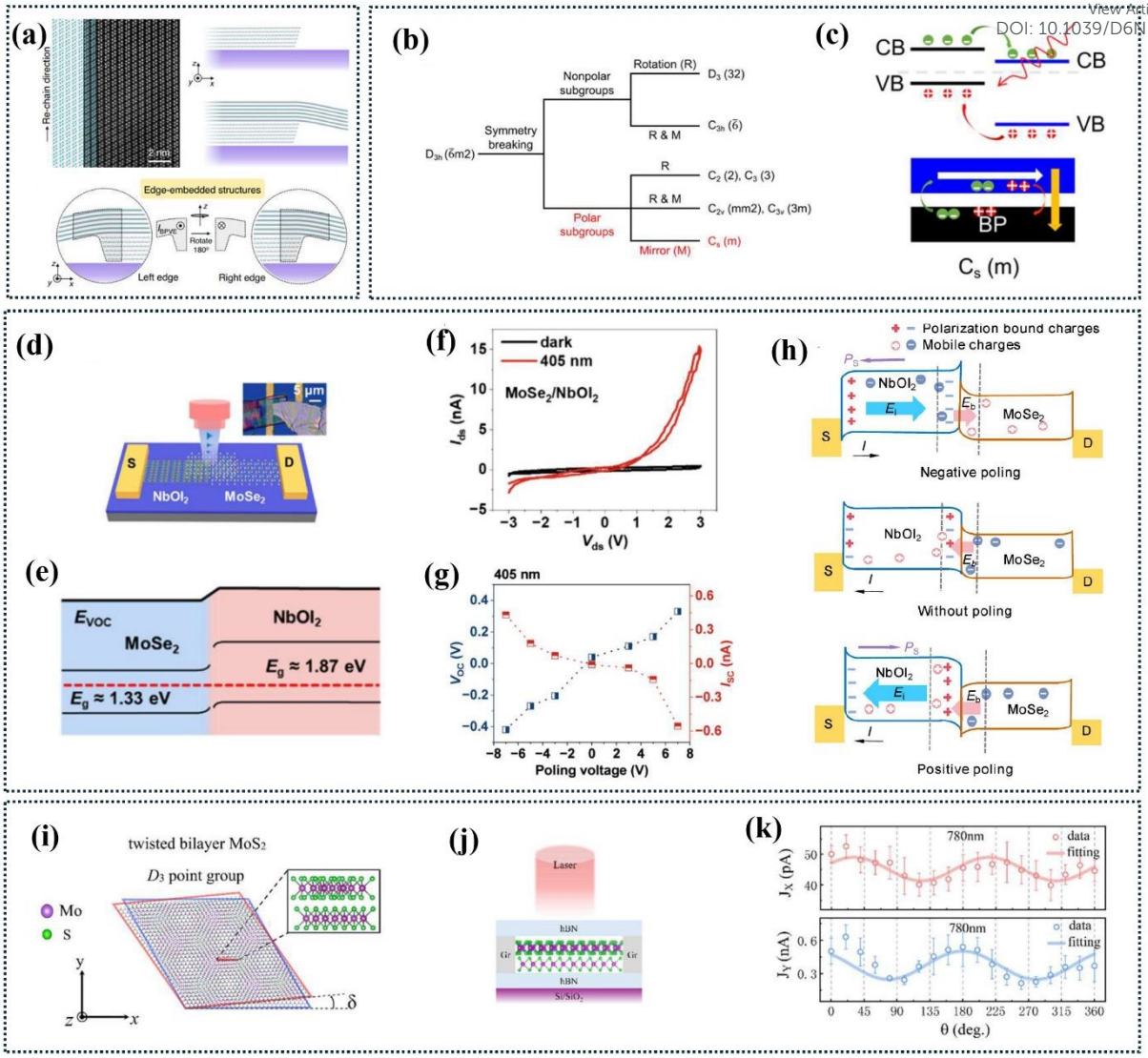

Fig. 9 ***Heterojunction, heterostructure, and twist layer.*** (a) On top left, schematics of vdW edge-embedded structures with STEM; on top right, Cross-sectional schematic of nano edges vdW layered materials, and on bottom, cross-sectional schematic of edge-embedded vdW homo- or hetero-structures. (b) Five polar groups can be obtained by breaking the D_{3h} symmetry in monolayer TMDC for the BPVE; (c) Polarization-induced increased band bending in TMDC/BP heterostructure and improved charge separation. (d) schematic of a self-powered photodetector made of a $MoSe_2/NbOI_2$ heterojunction, (e) corresponding schematic energy band structure of the $MoSe_2/NbOI_2$ heterojunction; (f) I−V properties of the $NbOI_2$ device in the dark and under 405 nm light, (g) I_{SC} and V_{OC} extracted after different voltage poling under 405 nm light. (h) Schematic of the self-powered working principle, where P_s is the direction of spontaneous polarization, E_b is the direction of the built-in electric field, and E_i is the internal electric field associated with ferroelectric polarization. (i) Twisted-angle MoS_2 forms the moiré superlattice structure; (j) Schematic diagram of the test for stacked twisted-angle MoS_2; (k) Polarization phase changes of the photocurrent in the X and Y directions when excited by a 780 nm laser.

Panel (a) reproduced from the Ref. [108], copyright 2023 Springer Nature; Panels (b) and (c) reproduced from the Ref. [104], copyright 2024 Springer Nature; Panels (d) to (h) reproduced from the Ref. [109],

copyright 2025 American Chemical Society; Panels (i) to (k) reproduced from the Ref. [105], copyright 2025 AIP publishing house.

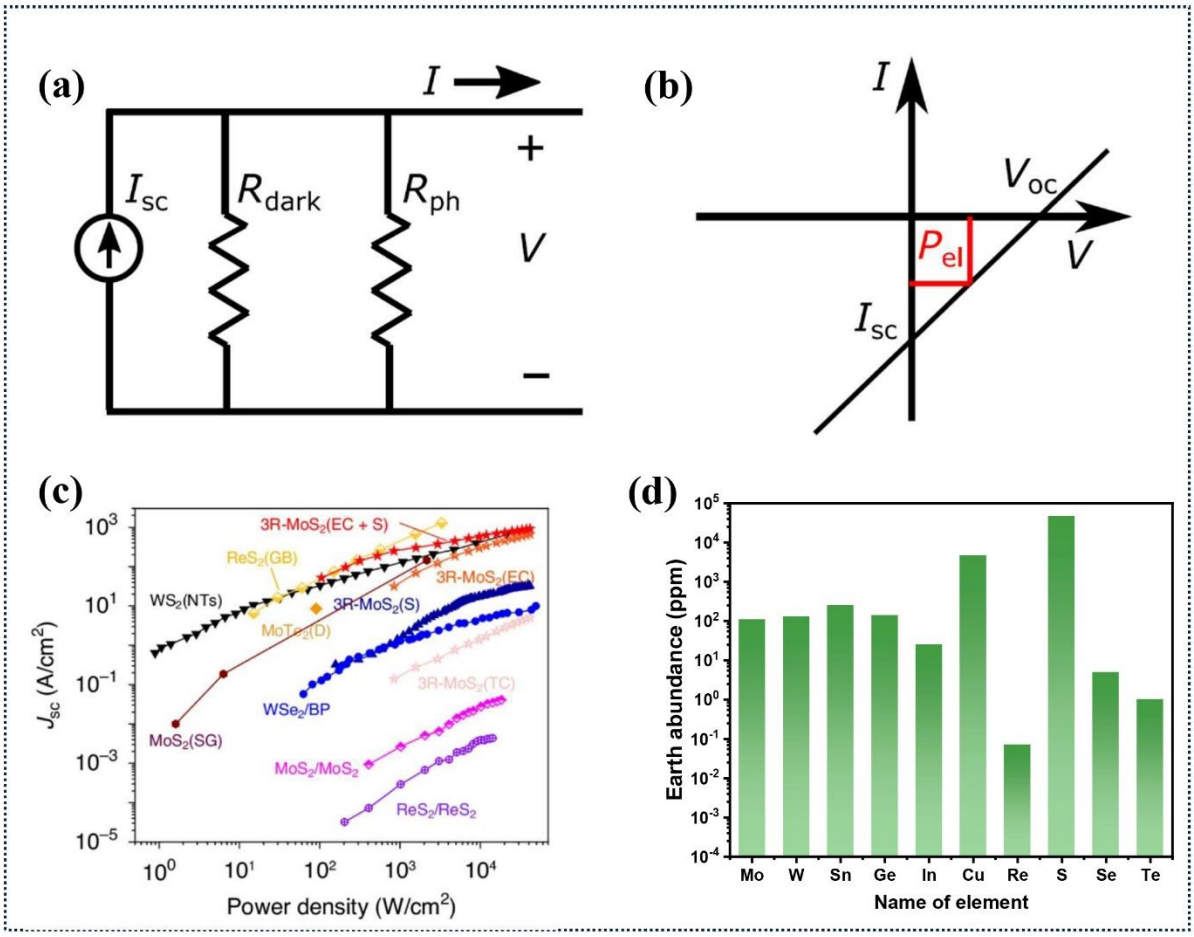

Fig. 10 (a) Circuit diagram of a BPVE cell showing the current source I_{SC} and parallel resistors R_{dark} and R_{ph}; (b) Linear *I-V* curve of BPVE raised from the shift current mechanism, and maximal extractable electrical power P_{el}, illustrating the fill factor of 25%. (c) The power density-dependence of BPVE J_{SC} in reported TMDs. (d) The abundance of various elements in vdW materials (1×10^{-6} wt%, ppm) exhibits BPVE.

Panels (a) and (b) reproduced from the Ref. [30], copyright 2023 American Physical Society; Panel (c) reproduced from the Ref. [47], copyright 2025 Springer Nature.

View Article Online
DOI: 10.1039/D6NH00127K

References:

1 L. Y. Gan, Q. Zhang, Y. Cheng and U. Schwingenschlögl, Photovoltaic heterojunctions of fullerenes with MoS2 and WS2 monolayers, *J. Phys. Chem. Lett.*, 2014, **5**, 1445–1449.

2 S. Nadupalli, J. Kreisel and T. Granzow, Increasing bulk photovoltaic current by strain tuning, *Sci. Adv.*, 2019, **5**, eaau9199.

3 S. Y. Yang, J. Seidel, S. J. Byrnes, P. Shafer, C. H. Yang, M. D. Rossell, P. Yu, Y. H. Chu, J. F. Scott, J. W. Ager, L. W. Martin and R. Ramesh, Above-bandgap voltages from ferroelectric photovoltaic devices, *Nat. Nanotechnol.*, 2010, **5**, 143–147.

4 W. Shockley and H. J. Queisser, Detailed Balance Limit of Efficiency of Broadband-Pumped Lasers, *J. Appl. Phys.*, 1961, **32**, 510–519.

5 L. Z. Tan, F. Zheng, S. M. Young, F. Wang, S. Liu and A. M. Rappe, Shift current bulk photovoltaic effect in polar materials—hybrid and oxide perovskites and beyond, *npj Comput. Mater.*, 2016, **2**, 16026.

6 H. Guan, N. Tang, X. Xu, L. Shang, W. Huang, L. Fu, X. Fang, J. Yu, C. Zhang, X. Zhang, L. Dai, Y. Chen, W. Ge and B. Shen, Photon wavelength dependent valley photocurrent in multilayer MoS2, *Phys. Rev. B*, 2017, **96**, 241304(R).

7 J. Wu, D. Yang, J. Liang, M. Werner, E. Ostroumov, Y. Xiao, K. Watanabe, T. Taniguchi, J. I. Dadap, D. Jones and Y. Ziliang, Ultrafast response of spontaneous photovoltaic effect in 3R-MoS2–based heterostructures, *Sci. Adv.*, 2022, **8**, eade3759.

8 A. G. Chynoweth, Surface space charge layers in Barium Titanate, *Phys. Rev.*, 1956, **102**, 705–714.

9 F. S. Chen, Optically induced change of refractive indices in LiNbO3 and LiTaO3, *J. Appl. Phys.*, 1969, **40**, 3389–3396.

10 A. M. Glass, D. Von Der Linde and T. J. Negran, High-voltage bulk photovoltaic effect and the photorefractive process in LiNbO3, *Appl. Phys. Lett.*, 1974, **25**, 233–235.

11 W. T. . Koch, R. Munser, W. Ruppel and P. Wurfel, Bulk photovoltaic effect in BaTiO3, *Solid State Commun.*, 1975, **17**, 847–850.

12 W. Ji, K. Yao and Y. C. Liang, Bulk photovoltaic effect at visible wavelength in epitaxial ferroelectric BiFeO3 thin films, *Adv. Mater.*, 2010, **22**, 1763–1766.

13 Z. Gu, D. Imbrenda, A. L. Bennett-Jackson, M. Falmbigl, A. Podpirka, T. C. Parker, D. Shreiber, M. P. Ivill, V. M. Fridkin and J. E. Spanier, Mesoscopic Free Path of Nonthermalized Photogenerated Carriers in a Ferroelectric Insulator, *Phys. Rev. Lett.*, 2017, **118**, 1–5.

14 J. E. Spanier, V. M. Fridkin, A. M. Rappe, A. R. Akbashev, A. Polemi, Y. Qi, Z. Gu, S. M. Young, C. J. Hawley, D. Imbrenda, G. Xiao, A. L. Bennett-Jackson and C. L. Johnson, Power conversion efficiency exceeding the Shockley-Queisser limit in a ferroelectric insulator, *Nat. Photonics*, 2016, **10**, 611–616.

15 A. Bhatnagar, A. Roy Chaudhuri, Y. Heon Kim, D. Hesse and M. Alexe, Role of domain walls in the abnormal photovoltaic effect in BiFeO3, *Nat. Commun.*, 2013, **4**, 2835.

16 Y. Zhang, S. Li, Y. Jiao, X. Wang, F. Gao, F. Bo, J. Xu and G. Zhang, Thickness-dependent photovoltaic effect in monocrystalline lithium niobate films of nanoscale

View Article Online
DOI: 10.1039/D6NH00127K

thickness, *Phys. Rev. Appl.*, 2024, **21**, 1.

17 S. Aftab, M. Z. Iqbal, Z. Haider, M. W. Iqbal, G. Nazir and M. A. Shehzad, Bulk Photovoltaic Effect in 2D Materials for Solar-Power Harvesting, *Adv. Opt. Mater.*, 2022, **10**, 2201288.

18 S. Kim, M. Kim and H. Kim, Self-powered photodetectors based on two-dimensional van der Waals semiconductors, *Nano Energy*, 2024, **127**, 109725.

19 S. Aftab and A. L. Moore, Engineering Bulk Photovoltaic Effect in 2D Transition Metal Dichalcogenides, *Adv. Sci.*, 2025, **2025**, e14337.

20 K. Kushnir, M. Wang, P. D. Fitzgerald, K. J. Koski and L. V. Titova, Ultrafast Zero-Bias Photocurrent in GeS Nanosheets: Promise for Photovoltaics, *ACS Energy Lett.*, 2017, **2**, 1429–1434.

21 D. Yang, J. Wu, B. T. Zhou, J. Liang, T. Ideue, T. Siu, K. M. Awan, K. Watanabe, T. Taniguchi, Y. Iwasa, M. Franz and Z. Ye, Spontaneous-polarization-induced photovoltaic effect in rhombohedrally stacked MoS2, *Nat. Photonics*, 2022, **16**, 469–474.

22 M. Ramos, T. Ahmed, B. Q. Tu, E. Chatzikyriakou, L. Olano-Vegas, B. Martín-García, M. R. Calvo, S. S. Tsirkin, I. Souza, F. Casanova, F. de Juan, M. Gobbi and L. E. Hueso, Unveiling Intrinsic Bulk Photovoltaic Effect in Atomically Thin ReS2, *Nano Lett.*, 2024, **24**, 14728–14735.

23 Y. Bai, W. Hao, Y. Wang, J. Tian, C. Wang, Y. Lei, Y. Yang, X. Yao, Q. Liu, C. Li, M. Gu and J. Wang, Anomalous Photocurrent Reversal for the Same Polarization Direction in van der Waals Ferroelectric CuInP2S6, 2024, DOI: 10.1103/prxenergy.3.023004.

24 S. M. Nahid, S. W. Nam and A. M. van der Zande, Depolarization Field-Induced Photovoltaic Effect in Graphene/α-In2Se3/Graphene Heterostructures, *ACS Nano*, 2024, **18**, 14198–14206.

25 X. Wu, L. Qi, M. A. Iqbal, S. Dai, X. Weng, K. Wu and C. Kang, Revealing Strong Flexoelectricity and Optoelectronic Coupling in 2D Ferroelectric CuInP2S6 Via Large Strain Gradient, *ACS Appl. Mater. Interfaces*, 2024, **16**, 14038–14046.

26 Y. Dong, M. M. Yang, M. Yoshii, S. Matsuoka, S. Kitamura, T. Hasegawa, N. Ogawa, T. Morimoto, T. Ideue and Y. Iwasa, Giant bulk piezophotovoltaic effect in 3R-MoS2, *Nat. Nanotechnol.*, 2023, **18**, 36–41.

27 C. L. Zhang, T. Liang, Y. Kaneko, N. Nagaosa and Y. Tokura, Giant Berry curvature dipole density in a ferroelectric Weyl semimetal, *npj Quantum Mater.*, 2022, **7**, 1–6.

28 B. Sturman and V. Fridkin, *Photovoltaic and photo-refractive effects in noncentrosymmetric materials*, Routledge, London, 1st Editio., 2021.

29 A. Avdoshkin, J. Mitscherling and J. E. Moore, Multistate Geometry of Shift Current and Polarization, *Phys. Rev. Lett.*, 2025, **135**, 66901.

30 A. Pusch, U. Römer, D. Culcer and N. J. Ekins-Daukes, Energy Conversion Efficiency of the Bulk Photovoltaic Effect, *PRX Energy*, 2023, **2**, 013006.

31 K. T. Butler, J. M. Frost and A. Walsh, Environmental Science Ferroelectric materials for solar energy conversion: photoferroics revisited, *Energy Environ. Sci.*, 2015, **8**, 838–848.

32 A. Alexandradinata, Quantization of intraband and interband Berry phases in the shift

View Article Online
DOI: 10.1039/D6NH00127K

current, *Phys. Rev. B*, 2024, **110**, 75159.

33 Y. Sheng, I. Fina, M. Gospodinov and J. Fontcuberta, Bulk photovoltaic effect modulated by ferroelectric polarization back-switching, *Appl. Phys. Lett.*, 2022, **120**, 242901.

34 M. Nakamura, S. Horiuchi, F. Kagawa, N. Ogawa, T. Kurumaji, Y. Tokura and M. Kawasaki, Shift current photovoltaic effect in a ferroelectric charge-transfer complex, *Nat. Commun.*, 2017, **8**, 281.

35 U. Dey, J. Van Den Brink and R. Ray, Correlation between electronic polarization and shift current in cubic and hexagonal semiconductors LiZn X (X = P , As , Sb), *Phys. Rev. Mater.*, 2024, **8**, 025001.

36 A. Kazempour, E. T. Sisakht, M. S. Okyay, X. Jiang, S. Sato, J. Oh and N. Park, Multistate control of nonlinear photocurrents in ferroelectric IV- monochalcogenide monolayers via phase manipulation of the light field, *Commun. Phys.*, 2025, **8**, 434.

37 N. A. Spaldin, A beginners guide to the modern theory of polarization, *J. Solid State Chem.*, 2012, **195**, 2–10.

38 J. Xin, Y. Guo and Q. Wang, Screening two-dimensional pyroelectric materials based on pentagonal chains with large shift current, *Phys. Rev. Mater.*, 2023, **7**, 1–7.

39 R. von Baltz and W. Krau, Theory of the bulk photovoltaic effect in pure crystals, *Phys. Rev. B*, 1981, **23**, 5590–5596.

40 Y. J. Zhang, T. Ideue, M. Onga, F. Qin, R. Suzuki, A. Zak, R. Tenne, J. H. Smet and Y. Iwasa, Enhanced intrinsic photovoltaic effect in tungsten disulfide nanotubes, 2019, DOI: 10.1038/s41586-019-1303-3.

41 D. Xiao, G. Bin Liu, W. Feng, X. Xu and W. Yao, Coupled spin and valley physics in monolayers of MoS2 and other group-VI dichalcogenides, *Phys. Rev. Lett.*, 2012, **108**, 196802.

42 H. Zeng, J. Dai, W. Yao, D. Xiao and X. Cui, Valley polarization in MoS2 monolayers by optical pumping, *Nat. Nanotechnol.*, 2012, **7**, 490–493.

43 K. F. Mak, K. L. McGill, J. Park and P. L. McEuen, The valley hall effect in MoS2 transistors, *Science (80-.).*, 2014, **344**, 1489–1492.

44 Y. Li, J. Fu, X. Mao, C. Chen, H. Liu, M. Gong and H. Zeng, Enhanced bulk photovoltaic effect in two-dimensional ferroelectric CuInP2S6, *Nat. Commun.*, 2021, **12**, 1–7.

45 Z. Tan, L. Hong, Z. Fan, J. Tian, L. Zhang, Y. Jiang, Z. Hou, D. Chen, M. Qin, M. Zeng, J. Gao, X. Lu, G. Zhou, X. Gao and J. M. Liu, Thinning ferroelectric films for high-efficiency photovoltaics based on the Schottky barrier effect, *NPG Asia Mater.*, 2019, **11**, 20.

46 X. Chen, K. Xu, T. Qin, Y. Wang, Q. Xiong and H. Liu, Bulk photovoltaic effect in a two-dimensional ferroelectric semiconductor α-In2Se3, *Nanoscale*, 2025, **17**, 5005–5011.

47 S. Qiao, J. Liu, C. Yao, N. Yang, F. Zheng, W. Meng, P. C. Y. Chow, D. Ki, L. Zhang, Y. Shi and L. Li, Boosting bulk photovoltaic effect in transition metal dichalcogenide by edge semimetal contact, *Light Sci. Appl.*, 2025, **14**, 22.

48 Y.-R. Chang, R. Nanae, S. Kitamura, T. Nishimura, H. Wang, Y. Xiang, K. Shinokita, K. Matsuda, T. Taniguchi, K. Watanabe and K. Nagashio, Shift-Current Photovoltaics

Based on a Non Centrosymmetric Phase in In-Plane Ferroelectric SnS, *Adv. Mater.*, 2023, **35**, 2301172.

49 V. K. Sangwan, D. G. Chica, T. C. Chu, M. Cheng, M. A. Quintero, S. Hao, C. E. Mead, H. Choi, R. Zu, J. Sheoran, J. He, Y. Liu, E. Qian, C. C. Laing, M. A. Kang, V. Gopalan, C. Wolverton, V. P. Dravid, L. J. Lauhon, M. C. Hersam and M. G. Kanatzidis, Bulk photovoltaic effect and high mobility in the polar 2D semiconductor SnP2Se6, *Sci. Adv.*, 2024, **10**, 1–9.

50 N. T. Kaner, Y. Wei, Y. Jiang, W. Li, X. Xu, K. Pang, X. Li, J. Yang, Y. Y. Jiang, G. Zhang and W. Q. Tian, Enhanced Shift Currents in Monolayer 2D GeS and SnS by Strain-Induced Band Gap Engineering, *ACS Omega*, 2020, **5**, 17207–17214.

51 H. G. Min, C. Lyi and Y. Kim, Tunable bulk photovoltaic effect in strained γ -GeSe, *Phys. Rev. B*, 2022, **106**, 205153.

52 B. Bian, Z. Wang, L. Zhang and Z. Yu, Photogalvanic-effect-induced generation of simultaneous charge and spin currents in a four-probe monolayer MoS2device, *Phys. Rev. Appl.*, 2026, **25**, 14003.

53 F. He, D. Chen, X. Ren, S. Meng and L. He, Ultrafast shift current dynamics in WS2 monolayer, *Phys. Rev. Res.*, 2024, **6**, 1–8.

54 R. Fei, W. Li, J. Li and L. Yang, Giant piezoelectricity of monolayer group IV monochalcogenides: SnSe, SnS, GeSe, and GeS, *Appl. Phys. Lett.*, 2015, **107**, 173104.

55 R. Fei, W. Kang and L. Yang, Ferroelectricity and Phase Transitions in Monolayer Group-IV Monochalcogenides, *Phys. Rev. Lett.*, 2016, **117**, 097601.

56 L. C. Gomes and A. Carvalho, Phosphorene analogues: Isoelectronic two-dimensional group-IV monochalcogenides with orthorhombic structure, *Phys. Rev. B*, 2015, **085406**, 1–8.

57 Z. F. Z. Li, Y.Xiao, Y. Gong, Z. Wang, Y. Kang, S. Zu, P. M. Ajayan, P. Nordlander, Active light control of the MoS2 Monolayer Exciton Binding Energy, *ACS Nano*, 2015, **9**, 10158–10164.

58 B. Zhu, X. Chen and X. Cui, Exciton binding energy of monolayer WS2, *Sci. Rep.*, DOI:10.1038/srep09218.

59 K. R. Hansen, J. S. Colton and L. Whittaker-Brooks, Measuring the Exciton Binding Energy: Learning from a Decade of Measurements on Halide Perovskites and Transition Metal Dichalcogenides, *Adv. Opt. Mater.*, 2024, **12**, 1–36.

60 J. J. Esteve-Paredes, M. A. García-Blázquez, A. J. Uría-Álvarez, M. Camarasa-Gómez and J. J. Palacios, Excitons in nonlinear optical responses: shift current in MoS2 and GeS monolayers, *npj Comput. Mater.*, 2025, **11**, 13.

61 H. Ai, Y. Kong, D. Liu, F. Li, J. Geng, S. Wang, K. H. Lo and H. Pan, 1T''' Transition-Metal Dichalcogenides: Strong Bulk Photovoltaic Effect for Enhanced Solar-Power Harvesting, *J. Phys. Chem. C*, 2020, **124**, 11221–11228.

62 R.-C. Xiao, Y. Gao, H. Jiang, W. Gan, C. Zhang and H. Li, Non-synchronous bulk photovoltaic effect in two-dimensional interlayer-sliding ferroelectrics, *npj Comput. Mater.*, 2022, **8**, 138.

63 M. Massicotte, P. Schmidt, F. Vialla, K. G. Schädler, K. Watanabe, T. Taniguchi, K. J. Tielrooij and F. H. L. Koppens, Picosecond photoresponse in van der Waals heterostructures, *Nat. Nanotechnol.*, 2016, **11**, 42–46.

64 J. Wang, N. Han, Z. Lin, S. Hu, R. Tian, M. Zhang, Y. Zhang, J. Zhao and X. Gan, A giant intrinsic photovoltaic effect in atomically thin ReS2, *Nanoscale*, 2024, **16**, 3101–3106.

65 A. M. Schankler, L. Gao and A. M. Rappe, Large Bulk Piezophotovoltaic Effect of Monolayer 2H-MoS2, *J. Phys. Chem. Lett.*, 2021, **12**, 1244–1249.

66 B. Kim, N. Park and J. Kim, Giant bulk photovoltaic effect driven by the wall-to-wall charge shift in WS2 nanotubes, *Nat. Commun.*, 2022, **13**, 3237.

67 F. Li, W. Wei, H. Wang, B. Huang, Y. Dai and T. Jacob, Intrinsic Electric Field-Induced Properties in Janus MoSSe van der Waals Structures, *J. Phys. Chem. Lett.*, 2019, **10**, 559–565.

68 C. Liu, T. Liang, X. Sui, L. Du, Q. Guo, G. Xue, C. Huang, Y. You, G. Yao, M. Zhao, J. Yin, Z. Sun, H. Hong, E. Wang and K. Liu, Anomalous photovoltaics in Janus MoSSe monolayers, *Nat. Commun.* , 2025, **16**, 1–7.

69 N. Sun, H. Ye, R. Quhe, Y. Liu and M. Wang, Prediction of photogalvanic effect enhancement in Janus transition metal dichalcogenide monolayers induced by spontaneous curling, *Appl. Surf. Sci.*, 2023, **619**, 156730.

70 H. Xu, H. Wang, J. Zhou, Y. Guo, J. Kong and J. Li, Colossal switchable photocurrents in topological Janus transition metal dichalcogenides, *npj Comput. Mater.*, 2021, **7**, 1–9.

71 J. Nag, S. Sarker, S. Imam, A. Iyer, M. J. Waters, A. Suceava, J. M. Rondinelli, M. G. Kanatzidis and V. Gopalan, Large Non-Resonant Infrared Optical Second Harmonic Generation in Bulk Crystals of Van der Waals Semiconductor, SnP2Se6, *Adv. Opt. Mater.*, 2025, **13**, 2402649.

72 N. Urakami, S. Ozaki and Y. Hashimoto, Bulk photovoltaic effect of an alpha-phase indium selenide (α-In2Se3) crystal along the out-of-plane direction, *Appl. Phys. Lett.*, DOI:10.1063/5.0222926.

73 Z. Xu, Y. Wang, Y. Cheng, Z. Zeng, L. Huang, C. Niu, Z. Liu, Z. Zhang, Y. Zhou and X. Wang, Thickness-Dependent Bulk Photovoltaic Effect and Ultrafast Response in 3R-MoS2, *Adv. Phys. Res.*, 2025, **4**, e00101.

74 H. Weyl, Elektron und Gravitation. I, *Zeitschrift für Phys.*, 1929, **56**, 330–352.

75 R. Vocaturo, K. Koepernik, J. I. Facio, C. Timm, I. C. Fulga, O. Janson and J. Van Den Brink, Electronic structure of the surface-superconducting Weyl semimetal PtBi2, *Phys. Rev. B*, 2024, **110**, 54504.

76 S. Ganeshan and S. Das Sarma, Constructing a Weyl semimetal by stacking one-dimensional topological phases, *Phys. Rev. B - Condens. Matter Mater. Phys.*, 2015, **91**, 1–11.

77 X. Wan, A. M. Turner, A. Vishwanath and S. Y. Savrasov, Topological semimetal and Fermi-arc surface states in the electronic structure of pyrochlore iridates, *Phys. Rev. B*, 2011, **83**, 1–9.

78 M. Guan, E. Wang, P. You, J. Sun and S. Meng, Manipulating Weyl quasiparticles by orbital-selective photoexcitation in WTe2, *Nat. Commun.*, 2021, **12**, 1885.

79 H. Weng, C. Fang, Z. Fang, B. Andrei Bernevig and X. Dai, Weyl semimetal phase in noncentrosymmetric transition-metal monophosphides, *Phys. Rev. X*, 2015, **5**, 1–10.

80 Y. Wang, X. Zhang, C. Li, X. Yao, R. Duan, T. K. M. Graham, Z. Liu, F. Tafti, D.

Broido, Y. Ran and B. B. Zhou, Visualization of bulk and edge photocurrent flow in anisotropic Weyl semimetals, DOI:10.1038/s41567-022-01898-0.

81 J. Lai, Y. Liu, J. Ma, X. Zhuo, Y. Peng, W. Lu, Z. Liu, J. Chen and D. Sun, Broadband Anisotropic Photoresponse of the 'hydrogen Atom' Version Type-II Weyl Semimetal Candidate TaIrTe4, *ACS Nano*, 2018, **12**, 4055–4061.

82 Q. Ma, S. Xu, C. Chan, C. Zhang, G. Chang, Y. Lin, W. Xie, T. Palacios, H. Lin, S. Jia, P. A. Lee, P. Jarillo-herrero and N. Gedik, Direct optical detection of Weyl fermion chirality in a topological semimetal, *Nat. Phys.*, 2017, **13**, 842–448.

83 C. Chan, N. H. Lindner, G. Refael and P. A. Lee, Photocurrents in Weyl semimetals, *Phys. Rev. B*, 2017, **95**, 041104(R).

84 A. K. Wu, D. Guerci, Y. Fu, J. H. Wilson and J. H. Pixley, Absence of quantization in the circular photogalvanic effect in disordered chiral Weyl semimetals, *Phys. Rev. B*, 2024, **110**, 14201.

85 J. Ma, Q. Gu, Y. Liu, J. Lai, P. Yu, X. Zhuo, Z. Liu, J. Chen, J. Feng and D. Sun, Nonlinear photoresponse of type-II Weyl semimetals, *Nat. Mater.*, 2019, **18**, 476–481.

86 S. Lim, C. R. Rajamathi, V. Süß, C. Felser and A. Kapitulnik, Temperature-induced inversion of the spin-photogalvanic effect in WTe2 and MoTe2, *Phys. Rev. B*, 2018, **98**, 1–5.

87 G. B. Osterhoudt, L. K. Diebel, M. J. Gray, X. Yang, J. Stanco, X. Huang, B. Shen, N. Ni, P. J. W. Moll, Y. Ran and K. S. Burch, Colossal mid-infrared bulk photovoltaic effect in a type-I Weyl semimetal, *Nat. Mater.*, 2019, **18**, 471–476.

88 Q. Wang, J. Zheng, Y. He, J. Cao, X. Liu, M. Wang, J. Ma, J. Lai, H. Lu, S. Jia, D. Yan, Y. Shi, J. Duan, J. Han, W. Xiao, J. Chen, K. Sun, Y. Yao and D. Sun, Robust edge photocurrent response on layered type II Weyl semimetal WTe2, *Nat. Commun.*, 2019, **10**, 5736.

89 J. Ma, B. Cheng, L. Li, Z. Fan, H. Mu, J. Lai, X. Song, D. Yang, J. Cheng, Z. Wang, C. Zeng and D. Sun, Unveiling Weyl-related optical responses in semiconducting tellurium by mid-infrared circular photogalvanic effect, *Nat. Commun.*, 2022, **13**, 5425.

90 X. Jia, R. Guo, J. Chen and X. Yan, Flexoelectric Effect in Thin Films: Theory and Applications, *Adv. Funct. Mater.*, 2025, **35**, 1–31.

91 S. Aftab, M. Z. Iqbal, M. W. Iqbal and M. A. Shehzad, Strain-Enhanced Photovoltaic Effect in MoTe2, *Laser Photon. Rev.*, 2023, **17**, 2200429.

92 T. Wu, K. Liu, S. Liu, X. Feng, X. Wang, L. Wang, Y. Qin and Z. L. Wang, Highly Efficient Flexocatalysis of Two-Dimensional Semiconductors, *Adv. Mater.*, 2023, **35**, 2208121.

93 J. Lee, G. Woo, J. Cho, S. Son, H. Shin, H. Seok, M. J. Kim, E. Kim, Z. Wang, B. Kang, W. J. Jang and T. Kim, Free-standing two-dimensional ferro-ionic memristor, *Nat. Commun.*, 2024, **15**, 5162.

94 W. Wang, Y. Xiao, T. Li, X. Lu, N. Xu and Y. Cao, Piezo-photovoltaic Effect in Monolayer 2H-MoS2, *J. Phys. Chem. Lett.*, 2024, **15**, 3549–3553.

95 C. Zhu, W. He, Z. R. Huang, B. Zhu, L. Q. Yue, P. Y. Huang, D. Li, J. Wang, L. Zhen, J. K. Qin and C. Y. Xu, Strain-Reduced Inversion Symmetry in Ultrathin SnP2Se6 Crystals for Giant Bulk Piezophotovoltaic Generation, *ACS Nano*, 2025, **19**, 2362–2370.

96 Z. Sun, J. Liu, N. Zhang, W. Shen, C. Hu, L. Li, F. Yan, F. Xia, H. Li, Y. Li and T. Zhai, Enhanced in-plane polarization in two-dimensional GaInS3 via strain engineering for self-powered photodetector, *Trans. Mater. Res.*, 2025, **1**, 100009.

97 S. Aftab, M. A. Shehzad, H. Muhammad, S. Ajmal, F. Kabir, M. Z. Iqbal and A. A. Al-kahtani, Bulk Photovoltaic Effect in Two-Dimensional Distorted MoTe2, *ACS Nano*, 2023, **17**, 17884–17896.

98 J. Jiang, Z. Chen, Y. Hu, Y. Xiang, L. Zhang, Y. Wang, G. Wang and J. Shi, Flexo-photovoltaic effect in MoS2, *Nat. Nanotechnol.*, 2021, **16**, 894–901.

99 J. Yu, B. Huang, S. Yang, Y. Zhang, Y. Bai, C. Song and W. Ming, Flexoelectric Engineering of Bulk Photovoltaic Photodetector, *Nano Lett.*, 2024, **24**, 6337–6343.

100 R. Sun, Z. Hu, X. Zhao, M. Zha, J. Zhang, X. Chen and Z. Liu, Strain-Prompted Giant Flexo-Photovoltaic Effect in Two-Dimensional Violet Phosphorene Nanosheets, *ACS Nano*, 2024, **18**, 13298–13307.

101 Y. Takada, T. Takizawa, K. Kaneko and M. Takashiri, Flexo-photovoltaic effect in strained bismuth telluride thin films without substrate bending under light irradiation, *Ceram. Int.*, 2024, **50**, 35368–35375.

102 J. Yu, Y. Zhang, S. Yang, C. Song, S. Xu, B. Huang, Q. Wang and J. Li, Self-powered tunable photodetection via flexoelectric engineering of, *J. Mater.*, 2025, **11**, 101103.

103 C. Cheon, Z. Sun, J. Cao, J. Francisco, G. Marin, T. Taniguchi, M. Luisier and A. Kis, Disorder-induced bulk photovoltaic effect in a centrosymmetric van der Waals material, *npj 2D Mater. Appl.*, 2023, **7**, 74.

104 Z. Zeng, Z. Tian, Y. Wang, C. Ge, F. Strauß, K. Braun, P. Michel, L. Huang, G. Liu, D. Li, M. Scheele, M. Chen, A. Pan and X. Wang, Dual polarization-enabled ultrafast bulk photovoltaic response in van der Waals heterostructures, *Nat. Commun.*, 2024, **15**, 5355.

105 B. Huang, S. Li, B. Li, Y. Shan, J. Cheng, H. Chen, J. Liu and X. Xie, Phonon-mediated shift currents in twisted bilayer MoS2, *Appl. Phys. Lett.*, 2025, **127**, 082101.

106 N. Sun, Y. Sun, W. Zhou, H. Ye, R. Quhe, Y. Liu and Z. Chen, Photogalvanic Effect in the WSe2 Monolayer with Defects Generated by Electron-Beam Irradiation for Self-Powered 2D Photodetectors: A Computational Study, *ACS Appl. Nano Mater.*, 2025, **8**, 7967–7973.

107 N. Sun, H. Ye, W. Zhou, R. Yang, R. Quhe, Y. Liu and Z. Chen, Enhanced photogalvanic effect in MoSSe monolayer with grain boundaries, *Appl. Phys. Lett.*, 2023, **123**, 211107.

108 Z. Liang, X. Zhou, L. Zhang, X. Yu, Y. Lv, X. Song, Y. Zhou, H. Wang, S. Wang, T. Wang, P. P. Shum, Q. He, Y. Liu, C. Zhu, L. Wang and X. Chen, Strong bulk photovoltaic effect in engineered edge-embedded van der Waals structures, *Nat. Commun.*, 2023, **14**, 4230.

109 X. Huang, Q. Wang, K. Song, Q. Hu, H. Zhang, X. Gao, M. Long, J. Xu, Z. Chen, G. Zhou and B. Wu, In-Plane Bulk Photovoltaic Effect in a MoSe2/NbOI2 Heterojunction for Efficient Polarization-Sensitive Self-Powered Photodetection, *Nano Lett.*, 2025, **25**, 1495–1503.

110 S. Zhao, X. Tai, R. Xiao, Y. Feng, C. Tian, J. Liu, Y. Sui, Y. Zhang, H. Wang, J. Wang, Y. Chen and G. Yu, Tunable WSe2−MoSe2 Lateral Heterojunction Photodetector Based on Piezoelectric and Flexoelectric Effects, *ACS Appl. Mater.*

View Article Online
DOI: 10.1039/D6NH00127K

Interfaces, 2024, **16**, 67889–67899.

111 H. Zhou, Y. Wei, W. Luo, C. Tan, Z. Dou, Z. Hu, Q. Li and X. Zheng, Symmetry-breaking-engineered in-plane bulk photovoltaic effect in van der Waals WS2/CrOCl heterostructure, *RSC Adv.*, 2025, **15**, 25625–25632.

112 J. Xin and Y. Guo, Bulk Photovoltaic Effect in the Elemental Blue Phosphorus-Based Polar Homojunction and Heterojunction, *J. Phys. Chem. C*, 2024, **128**, 9705–9711.

113 Y. Gao, W. Zou and C. Zhang, The bulk photovoltaic effect in the one-dimensional interface of graphene/BN superlattices, *Phys. Chem. Chem. Phys.*, 2025, **27**, 22621–22628.

114 T. V Joya, T. Kawakami and M. Koshino, Shift current response in twisted double bilayer graphene, *Phys. Rev. B*, 2025, **112**, 85407.

115 C. Hua, M. H. Naika, Y.-H. Chana, J. Ruana and S. G. Louie, Light induced shift current vortex crystals in moiré heterobilayers, *Proc. Natl. Acad. Sci. U.S.A.*, 2023, **120**, e2314775120.

116 X. Fan, Y. Jiang, X. Zhuang, H. Liu, T. Xu, W. Zheng, P. Fan, H. Li, X. Wu, X. Zhu, Q. Zhang, H. Zhou, W. Hu, X. Wang, L. Sun, X. Duan and A. Pan, Broken Symmetry Induced Strong Nonlinear Optical Effects in Spiral WS2 Nanosheets, *ACS Nano*, 2017, **11**, 4892–4898.

117 S. Ghosh, Y. Zheng, Z. Zhang, Y. Sun, T. F. Schranghamer, N. U. Sakib, A. Oberoi, C. Chen, J. M. Redwing, Y. Yang and S. Das, Monolithic and heterogeneous three-dimensional integration of two-dimensional materials with high-density vias, *Nat. Electron.*, 2024, **7**, 892–903.

118 A. A. Yaroshevsky, Abundances of chemical elements in the Earth's crust, *Geochemistry Int.*, 2006, **44**, 48–55.

119 J. Li, X. Yang, Z. Zhang, W. Yang, X. Duan and X. Duan, Towards the scalable synthesis of two-dimensional heterostructures and superlattices beyond exfoliation and restacking, *Nat. Mater.*, 2024, **23**, 1326–1338.

View Article Online
DOI: 10.1039/D6NH00127K

Data Availability Statement

This article is a review of previously published studies. All data presented in tables and figures were derived from published literature, and the sources are cited within the article. No new primary data were generated or analyzed.